

1995/07798

N95- 14212

25-29

17016

p 19

THE SOLID SURFACE COMBUSTION EXPERIMENT
ABOARD THE USML-1 MISSION

Robert A. Altenkirch*, Kurt Sacksteder**, Subrata Bhattacharjee***,
Prashant A. Ramachandra*, Lin Tang*, and M. Katherine Wolverton*

* Department of Mechanical Engineering and the National Science Foundation Engineering Research
Center for Computational Field Simulation
Mississippi State University
Mississippi State, MS 39762

** NASA Lewis Research Center
Cleveland, OH 44135

*** Department of Mechanical Engineering
San Diego State University
San Diego, CA 92182

ABSTRACT

An experiment was conducted aboard STS-50/USML-1 in the solid Surface Combustion Experiment (SSCE) hardware for flame spread over a thin cellulosic fuel in a quiescent oxidizer of 35% oxygen / 65% nitrogen at 1.0 atm. pressure in microgravity. The USML-1 test was the fourth of five planned experiments for thin fuels, one performed during each of five Space Shuttle Orbiter flights. Data that were gathered include gas- and solid-phase temperatures and motion picture flame images. Observations of the flame are described and compared to theoretical predictions from steady and unsteady models that include flame radiation from CO₂ and H₂O.

Experimental results from the five experiments indicate that flame spread rate increases with increasing ambient oxygen content and pressure. The brightness of the flame and the visible soot radiation also increase with increasing spread rate. Steady-state numerical predictions of temperature and spread rate and flame structure trends compare well with experimental results near the flame leading edge while gradual flame evolution is captured through the unsteady model.

INTRODUCTION

Flame spread over solid fuels is a phenomenon of fundamental, scientific interest as well as one that has practical implications. The behavior of spreading flames is dependent on the environment and the flow field in which the phenomenon occurs, and so it is important to understand these effects in order

Joint "L+1" Science Review for USML-1 and USMP-1 with the Microgravity Measurement Group, September 22-24, 1993, Huntsville, Alabama, USA.

83

to develop effective fire suppression strategies. A unique environment in which flame spreading has importance to fire safety issues is that of spacecraft in which the gravitational acceleration is low compared to that of the Earth, here referred to as microgravity.

In normal gravity, induced flows due to buoyancy are present, and so it is difficult to control the flow field in which a spreading flame is embedded. Additionally, extrapolation of experimental and modeling results obtained from an environment in which buoyancy is present to one in which it is not is difficult if not impossible because the physics dominant in the two environments are not quite the same. Buoyancy induced flows are generally strong enough to suppress radiative effects, which prove to be important in the low-flow environments that is obtained in microgravity. As a result, a program of conducting flame spreading experiments in a quiescent, microgravity environment was established so that the physics of the flame spread process in that environment could be delineated without having to contend with the complicating effects of buoyancy.

The experiments were designed to be conducted aboard Space Shuttle Orbiter flights. Keeping in mind crew safety and development costs, the experimental hardware was designed for a single experiment per flight. Here we summarize results from the USML-1 experiment and provide some comparison with both steady and unsteady flame spread models and earlier experiments. Detailed results from and analyses of earlier flights can be found in several of the references listed here.

I. HARDWARE DESCRIPTION

The experiment described here was conducted aboard STS-50/USML-1 on 2 July 1992 using the Solid Surface Combustion Experiment (SSCE) payload specifically designed for these tests [1]. The SSCE chamber has a contained gas volume of 0.039 m^3 , two orthogonal windows, and a centrally located sample holder. The sample holder supports the fuel, three thermocouples, and a pressure transducer and was designed to withstand the stresses of a Shuttle launch.

A camera module includes two 16 mm motion picture cameras, using Kodak 7296 color negative film, ASA rated 500, an electronics box, and a battery box. The cameras are positioned so spreading flames cross the fields of view, one axis normal to the sample surface (top view), the other parallel (side view). The cameras provided a timing light strobe on the margin of the film to measure the framing rate, and a 1 Hz strobe light was used to illuminate the fuel surface to observe the propagation of the surface pyrolysis front. The experiment was filmed using a lens aperture of $f/1.4$.

The test sample, 11.0 cm long by 3.0 cm wide, was made from Whatman #1 filter paper, 0.0825 mm half-thickness with an area density, based on the half-thickness, of $4.282 \times 10^{-2} \text{ Kg/m}^2$. The sample was clamped between two thin metal sheets with both sides of the fuel exposed to the atmosphere. A nichrome ignitor wire with a webbed pattern, 1.0 cm long, was clipped over one end of the sample. A

solution of nitrocellulose in acetone was applied to the sample over the ignitor wire and allowed to dry. Three Type R thermocouples of 0.13 mm wire diameter were installed: 7.0 mm above the center of the sample, embedded in the center of the sample, and 2.3 mm below the sample 2.54 cm farther from the ignitor than the first two.

The experiment sequence is automated beginning with a five-second camera acceleration to 24 frames per second. The ignitor is then energized with 2 amps of current for five seconds. The thermocouple and pressure signals are recorded digitally at 20 Hz, and camera operation and data acquisition continue for 68 s after the ignitor is energized.

The film was forced-processed two f-stops. A color frame grabber was used to digitize the flame images, frame by frame. The images were spatially filtered to smooth the film grain, and an edge detection scheme based on the brightness of the blue component of the image was used to measure the flame position and calculate the flame spread rate. The experiment was conducted at 35% oxygen/65% nitrogen and 1.0 atm pressure, the lowest oxygen percentage. Earlier flight tests were conducted at 50% oxygen and 1-2 atm.

II. CONDUCT OF THE EXPERIMENT

The USML-1 flight of the SSCE hardware was its fourth. Payload Commander Bonnie Dunbar began the experiment on schedule, with assistance from Pilot Ken Bowersox. In earlier flights, STS-41 and STS-43, the crew used the Orbiter CCTV for a real-time down link of the flame image. Time was provided during the USML-1 mission to use the CCTV for real-time coverage of the top view of the fuel sample. The photographic shroud used to ensure a darkened chamber for the cine film worked well enough to saturate the CCTV automatic gain control. In consultation with the SSCE team in the POCC, Payload Commander Dunbar used a penlight to reflect enough light off the chamber exterior and into the CCTV to bring the detector out of saturation and provide a good video exposure. Ignition and flame spread was initiated, proceeded nominally, and the SSCE team was able to observe the pyrolysis front propagation in real time.

The flight film was recovered early from the Spacelab and taken by the SSCE team to the Johnson Space Center (JSC). The cine films were processed by the Imaging Sciences Division (ISD) at the JSC, using a procedure customized for this project. The JSC-ISD also provided a video transfer from the original film.

III. MODELING

Because details of the steady model have been described before [2,3], and the extension of the steady model to include unsteady effects is conceptually straightforward, although not without practical

difficulty [4], the discussion here is abbreviated. The model consists of the unsteady, two-dimensional continuity, momentum, species (fuel, oxygen, nitrogen), and energy equations in the gas, written in the common form

$$\frac{\partial(\rho\phi)}{\partial t} + \frac{\partial(\rho u\phi)}{\partial x} + \frac{\partial(\rho v\phi)}{\partial y} = \frac{\partial}{\partial x} \left[\Gamma_\phi \frac{\partial\phi}{\partial x} \right] + \frac{\partial}{\partial y} \left[\Gamma_\phi \frac{\partial\phi}{\partial y} \right] + S_\phi \quad (1)$$

where ϕ , Γ_ϕ and S_ϕ for the different equations are listed below,

	ϕ	Γ_ϕ	S_ϕ
<i>continuity</i>	1	0	0
<i>x-momentum</i>	u	μ	$-\partial P/\partial x$
<i>y-momentum</i>	v	μ	$-\partial P/\partial y$
<i>fuel</i>	m_f	μ/Pr	$-B_g \rho^2 m_f m_{ox} e^{-E_g/(RT)}$
<i>oxygen</i>	m_{ox}	μ/Pr	$s S_f$
<i>nitrogen</i>	m_{N_2}	μ/Pr	0
<i>energy</i>	T	μ/Pr	$\left[-\Delta H_c S_f + \dot{q}_{ign}''' - 4a_p \sigma (T^4 - T_\infty^4) \right] / C_p$

and the continuity and energy equations in the solid.

$$\dot{m}'' = \frac{d(\rho_s \tau)}{dt} = -A_s \rho_s \tau e^{-E_s/RT_s} \quad (2)$$

$$\frac{\partial(\rho_s C_s T \tau)}{\partial t} = -\dot{m}'' L_v + \lambda_s \frac{\partial T}{\partial y} l_g + \dot{q}_{ign}''' \tau \quad (3)$$

The term \dot{q}_{ign}''' in the gas- and solid-phase energy equations is the transient ignition term, and other symbols in Eqns. (1)-(3) are usual ones [2-4].

Viscosity and thermal conductivity at 700 K are $0.0515 \text{ W m}^{-1} \text{ K}^{-1}$ and $2.46 \times 10^{-5} \text{ kg m}^{-1} \text{ s}^{-1}$, respectively, for 50% oxygen, and $0.0508 \text{ W m}^{-1} \text{ K}^{-1}$ and $2.63 \times 10^{-5} \text{ kg m}^{-1} \text{ s}^{-1}$, respectively, for 35% oxygen and are varied with the square root of temperature for a fixed Prandtl number of 0.7 and unit Lewis number. Chemical reaction is a one-step, second-order Arrhenius process with a pre-exponential factor of $1.58 \times 10^{11} \text{ m}^3 \text{ kg}^{-1} \text{ s}^{-1}$ [2], activation energy of $1.167 \times 10^5 \text{ kJ kmol}^{-1}$ [2], and heat of combustion of $1.674 \times 10^4 \text{ kJ kg}^{-1}$ [5]. The specific heat of the gas is $1.465 \text{ kJ kg}^{-1} \text{ K}^{-1}$ [6] for 50%

oxygen and $1.352 \text{ kJ kg}^{-1} \text{ K}^{-1}$ for 35% oxygen. The source term in the gas-phase energy equation contains the chemical heat-release term, the transient ignition-energy input term, and a radiation loss term. The gas-phase radiation is modeled using a Planck absorption coefficient obtained from a detailed radiation calculation in the steady-state model that accounts for radiation from CO_2 and H_2O [3].

First-order Arrhenius kinetics, with pre-exponential factor of $7.8 \times 10^{16} \text{ s}^{-1}$ [2], and activation energy of $2.494 \times 10^5 \text{ kJ kmol}^{-1}$ [2], describe the fuel pyrolysis. The specific heat of the solid fuel and heat of vaporization are $1.256 \text{ kJ kg}^{-1} \text{ K}^{-1}$ [5] and $368.45 \text{ kJ kg}^{-1}$ [5], respectively. Surface reradiation and gas-to-surface radiative feedback are taken to balance for purposes here [7]. Unsteady fuel heating and the energy required for pyrolysis then are provided by conduction from the gas and from the transient ignition source.

The solid- and gas-phase equations are solved simultaneously and numerically, using the SIMPLER algorithm [8], for a 10 cm long sample in a domain 15 cm long by 10 cm above one side of the fuel. The domain is extended 2.3 cm behind the ignition end of the fuel sample, which allows oxygen to diffuse into this region to give rise to a trailing-edge flame. The other end of the fuel sample is extended by 2.7 cm and is inert with the properties of the metal holder in the experiment. The numerical domain is represented by a 92×40 uniform grid and a time step of 0.0165 s, except during the ignition transient when the time step is halved.

Computationally the flame spreads left to right across the domain atop the fuel surface. Boundary conditions on the left, right, and top of the domain are ambient pressure and zero gradients for all field variables. The fuel is within the computational domain such that the boundary condition at the bottom is that the fuel is insulated at its half-thickness; behind the fuel burnout is a slip plane. At the fuel gas interface, there is a no slip condition and diffusion-convection balances normal to the fuel for energy and species.

The 1 cm-long ignition source, $2 \times 10^8 \text{ W/m}^2$, is at the left end of the fuel sample and is turned on at the beginning of the simulation. The source is turned off once the flame develops, which is approximately at 1.2 s into the computation. The mean Planck absorption coefficient is increased linearly with time from zero until steady spread of the leading edge is achieved.

IV. RESULTS

A. Description of the Flame

Filmed images of the SSCE flames were recorded during each flight. The apparent brightness of the flames varies from nearly undetectable in this 35% oxygen case to near saturation, indicating enhanced soot production both with increasing atmospheric oxygen content and pressure, particularly at 50% oxygen. For 35% oxygen a flame image from the top is not detectable on film, but the 1 Hz strobe

light in the chamber allows the progress of the apparent pyrolysis front across the sample to be seen.

For the USML-1 experiment at 35% oxygen, the shape of the visible flame is symmetrical about the midpoint of its length, and, after the ignition transient, becomes steady with a maximum visible height of 0.5 cm and a length of 1.4 cm. A black-and-white print from one frame of the film is shown in Fig. 1.

Unlike the flames at 50% oxygen, which behind the leading edge curve away from the surface to a maximum distance (height) from the surface and then curve back toward the surface near the trailing edge, the 35% oxygen flame is nearly flat, curving very slightly toward the fuel surface near the leading and trailing edges as seen in Fig. 1. Additionally, the leading edge and trailing edge are equally bright, although the presence of the thermocouple in the frame of Fig. 1 obscures this fact somewhat.

In the top view, there is evidence that the fuel was not entirely consumed as the flame passed, as it would have been at 35% oxygen in normal gravity. This observation suggests that pyrolysis products may be available far behind the flame leading edge.

B. Spread Rate and Temperature Measurement

In the recorded flame images, the leading edge of the flame reaches a steady spread rate almost immediately following ignition, while the trailing edge, in general, develops more slowly. The nominal leading-edge spread rate determined from the film for the 35% oxygen/1.0 atm experiment here is 0.092 cm/s, while at 1.5 atm it is 0.150 cm/s, and at 50% oxygen, for 1.0, 1.5, and 2.0 atm it is 0.358, 0.454, and 0.547 cm/s, respectively. The measured temperatures are shown as a function of time in Fig. 2. Following an earlier error analysis of the thermocouple measurements [9], the reported temperatures are uncorrected. Because it was farther from the ignitor, the temperature history of the gas-phase thermocouple 2.3 mm from the surface is shown shifted in time by an amount equal to the displacement divided by the steady flame spread rate.

The surface temperature increases as the leading edge of the flame approaches the thermocouple, a plateau in temperature is nearly reached as the fuel pyrolyzes, and the temperature rises again as the trailing edge of the flame approaches. Following passage of the trailing edge, the temperature decreases. Because the maximum height of the visible flame above the surface is less than the distance of the thermocouple farthest (7.0 mm) from the surface, that thermocouple signal shows only a single peak in temperature. The thermocouple 2.3 mm from the surface senses only the leading edge of the flame prior to the time at which data taking ceases.

C. Steady-State Model Comparisons

The steady-state model developed in detail elsewhere [2,3,7] describes well the overall

characteristics of the leading edge of the flame, the flame region responsible for establishing the spread rate. Predicted surface temperatures there match well with experiment [7], the model predicts an increase in spread rate with pressure [7] and with increasing oxygen concentration, and a slight increase of pyrolysis temperature with increasing pressure [7]. As seen later, measured pyrolysis temperature increases with pressure for 35% oxygen, although that behavior is not quite as clear for 50% oxygen. In comparison, the expression for spread rate given by de Ris for heat-conduction-limited-spread over a thermally thin fuel [10] predicts a decrease in spread rate with increasing pressure due to the prediction from the steady model of a increase in vaporization temperature with pressure.

The predicted increase in spread rate with pressure, consistent with experiment and opposite of the thermal theory of de Ris, can be explained from gas-phase radiation effects. An increase in pressure results in an increase in Planck mean absorption coefficient computed as described in Ref. [3] and taking into account the distribution of temperature, CO_2 , and H_2O , but neglecting the presence of soot. Predicted absorption coefficients, used in the radiative source term in the gas-phase energy equation, increase from 1.9 m^{-1} at 1.0 atm, to 2.4 m^{-1} at 1.5 atm, to 3.0 m^{-1} at 2.0 atm and 50% oxygen, but a thinning of the reaction zone occurs with an increase in pressure such that the optical thickness of the flame decreases [7]. As a result, flame cooling due to radiation decreases with increasing pressure causing an increase in spread rate. Although this result was obtained neglecting radiative feedback to the surface, inclusion of radiative feedback as described in Ref. [3] did not change this conclusion. Neglecting that feedback is equivalent to assuming that the gas radiation to the surface is balanced by the surface reradiation or that the surface emittance and absorption are set equal to zero.

The steady model qualitatively predicts the overall size of the flame adequately. Temperature contours, in the units of the ambient temperature of 298 K, are shown in Fig. 3 for flames spreading left to right. For 35% oxygen, the dimensionless temperature of 3.0 encloses the experimental flame shown in Fig. 1. Superimposed on the temperature contours in Fig. 3 are the computed velocity vector fields for the 50%/2.0 atm flame and the 35%/1.0 atm USML-1 flame. The velocities are shown in units of computed spread rate. As in the experiments, the 50%/2.0 atm flame extends away from the surface the farthest, and the 35%/1.0 atm flame the least. Additionally, the experimental 35%/1.0 atm flame is nearly symmetrical about the midpoint of its length, which is evident in Fig. 1. The asymmetry evident for the 50%/2.0 atm case is consistent with the higher spread rate, which results in a higher relative velocity of oxidizer into the flame at the leading edge.

D. Unsteady Model Comparisons

While the steady model describes the character of the leading edge of the flame properly, it is unable to describe a trailing edge structure and the evolution of the trailing edge after the ignition

transient. The tendency of the flame to curve back toward the surface near the trailing edge is never adequately captured by the steady model. Increases in gas and surface temperature found experimentally as the trailing edge of the flame passes over the thermocouples are not predicted.

Predicted surface temperatures from the unsteady model for 35% oxygen are compared to the flight measurements in Fig. 4, and gas-phase temperatures are compared in Fig. 5. The structure of the profiles is generally captured by the unsteady model. Like the steady model, the unsteady results were obtained neglecting radiation feedback to the surface. For calculations of radiative loss to the surroundings, absorption coefficients at 35% were estimated from the computed values at 50%, correcting for the differences in CO_2 and H_2O produced from stoichiometric reaction at 35% as compared to 50%, to be 1.46 m^{-1} and 1.84 m^{-1} at 1.0 and 1.5 atm, respectively.

The flight experiments show that a substantial amount of solid fuel remains following the initial spreading of the gas-phase flame, while in normal gravity the same fuel is entirely consumed. The one-step, Arrhenius, pyrolysis model requires a dimensionless fuel density at burnout, defined as the ratio of the solid density at burnout to that of the virgin fuel. Reflecting the flight experiment observations, the burnout density was chosen to be 0.7 for 35% oxygen, i.e., only 30% of the potentially pyrolyzable fuel is converted to gas-phase fuel. This value of burnout density is much higher than the value of 0.27 than the pyrolysis experiments of Kushida *et al.* suggest [11], but burnout densities below 0.7 do not allow the observed structure of the trailing edge to evolve and result in flames that in the calculation are too long. With a burnout density of 0.27, the model predicts that the trailing edge does not move from the point of ignition for the entire experiment time, contrary to the observations.

Surface temperature and heat flux distributions computed from the unsteady model are shown in Fig. 6 for comparison to the experimental values, derived from the spread rate and temperature measurements, shown in Fig. 7. Surface radiation in both figures was computed from the surface temperature assuming a surface emittance of 0.5, and the remaining details of the data reduction scheme used to compute the experimental heat fluxes is described elsewhere [9]. In both figures, each distribution is normalized with its peak value, which is shown in parentheses in the figure legend.

Computationally, conduction constitutes the net heat flux to the solid, because surface radiation and gas-to-surface radiation are taken to balance. The computational net heat flux profile shows a single peak near the flame leading with a magnitude comparable to the experimental conduction peak, the two differing by about a factor of two. Experimentally, the net flux shows two peaks near the leading edge, which is due to the influence of radiation; conduction alone cannot account for this behavior. Surface radiation and gas-to-surface radiation are at least comparable in Fig. 7, consistent somewhat with the model assumption of a balance between the two. The magnitude of the radiative fluxes compared to conduction clearly indicates their importance, and the fact that the conduction flux and the gas-to-surface

radiative flux do not peak at the same location gives rise to the net heat flux profile observed experimentally.

For further comparison, computational results for 50% oxygen and 1.5 atm pressure are shown in Fig. 8, with the corresponding experimental results shown in Fig. 9. Behavior similar to the 35% oxygen flame is obtained, although more experimental data are available in the pyrolysis region, because of the higher spread rate, showing that surface radiation and gas-to-surface radiation there are comparable. The separation of the peaks of the conduction and gas-to-surface radiation fluxes, and the importance of the radiative flux near the leading edge, is evident in Fig. 9, which again gives rise to the character of the net heat flux profile different from a pure conduction process.

CONCLUSIONS

Flame spread over a thin solid fuel in a quiescent, microgravity environment was studied in one atmosphere aboard USML-1 in a continuing series of flight tests. Experimental results, along with results from a steady and an unsteady model, show generally that the flame elongates after ignition, forming a trailing edge that follows the leading edge at a slower speed. After a lengthy ignition transient, the flame shape is steady. The spread rate of the leading edge becomes steady almost immediately after ignition and increases with increasing pressure and oxygen content.

The brightness of the flames increases as the spread rate increases with atmospheric conditions, and the color of the flame changes from blue to orange, indicating increased soot production. The faster spreading flames are elongated and asymmetric, while the slower spreading flames, such as the USML-1 flame, are symmetrical about the midpoint of their length.

Trends in flame size, temperature, and spread rate are reproduced by the steady and unsteady models when radiation loss from the flame is included. However, trailing-edge phenomena, which appear to be inherently unsteady, are only captured by the unsteady model. The experiment observations suggest that the fuel is not completely pyrolyzed after the flame passes, and the fuel density at burnout, treated as a parameter, must be relatively high in order to obtain qualitative agreement between model and experiment.

Experimental heat flux profiles demonstrate the importance of radiative processes in these low-gravity flames. Conduction and radiative fluxes are comparable in magnitude, and although model predictions of conduction fluxes are quite comparable to experiment, coupling between surface and gas radiative processes is generally needed to predict the behavior of the experimental heat flux profiles near the flame leading edge. With basic flame structure and evolution predictable, submodel refinement, e.g., the degree of radiative coupling, will allow for more quantitative agreement between model and experiment to be pursued.

ACKNOWLEDGMENTS

This work was supported by NASA through Contract NAS3-23901. We thank Prof. S. V. Patankar for providing to us an initial version of the gas-phase software. We gratefully acknowledge the contributions of Ralph Zavesky, John Koudelka, and the SSCE flight hardware team at the NASA-Lewis Research Center and the program support of NASA Headquarters, Microgravity Division, Office of Space Science and Applications.

REFERENCES

1. Vento, D., Zavesky, R., Sacksteder, K., and Altenkirch, R. A., *The Solid Surface Combustion Space Shuttle Experiment Hardware Description and Ground-Based Test Results*, NASA TM 101963, 1989.
2. Bhattacharjee, S., and Altenkirch, R. A., *Twenty-Fourth Symposium (International) on Combustion*, The Combustion Institute, Pittsburgh, 1992, pp. 1669-1676.
3. Bhattacharjee, S., and Altenkirch, R. A., *Twenty-Third Symposium (International) on Combustion*, The Combustion Institute, Pittsburgh, 1990, pp. 1627-1633.
4. Bullard, D.B., Tang, L., Altenkirch, R. A., and Bhattacharjee, S., *Advances in Space Research.*, 13:(7)171-(7)184 (1993).
5. Altenkirch, R. A., Eichhorn, R. and Shang, P. C., *Combustion and Flame*, 37: 71-83, (1980).
6. West, J., Bhattacharjee, S., and Altenkirch, R. A., *Combustion Science and Technology*, 83: 233-244, (1992).
7. Bhattacharjee, S., Altenkirch, R. A., and Sacksteder, K., *ASME Winter Annual Meeting*, 1993.
8. Patankar, S. V., *Numerical Heat Transfer and Fluid Flow*, Hemisphere Publishing Corporation, New York, 1980.
9. Bhattacharjee, S., Altenkirch, R. A., and Sacksteder, K., *Combustion Science and Technology*, 91:225-242 (1993).
10. de Ris, J.N., *Twelfth Symposium (International) on Combustion*, The Combustion Institute, Pittsburgh, 1969, pp. 241-252.
11. Kushida, G., Baum, H. R., Kashiwagi, T., and di Blasi, C., *Journal of Heat Transfer*, 114: 494-502 (1992).

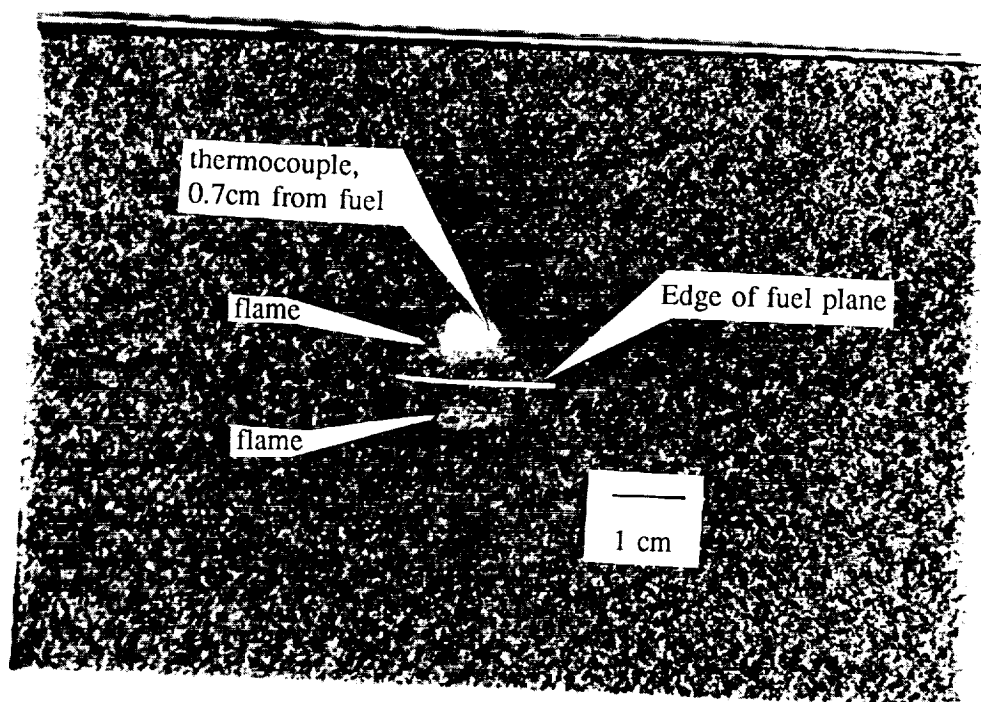


Figure 1 Black-and-white photograph of the flame spreading left to right at approximately half way along the sample.

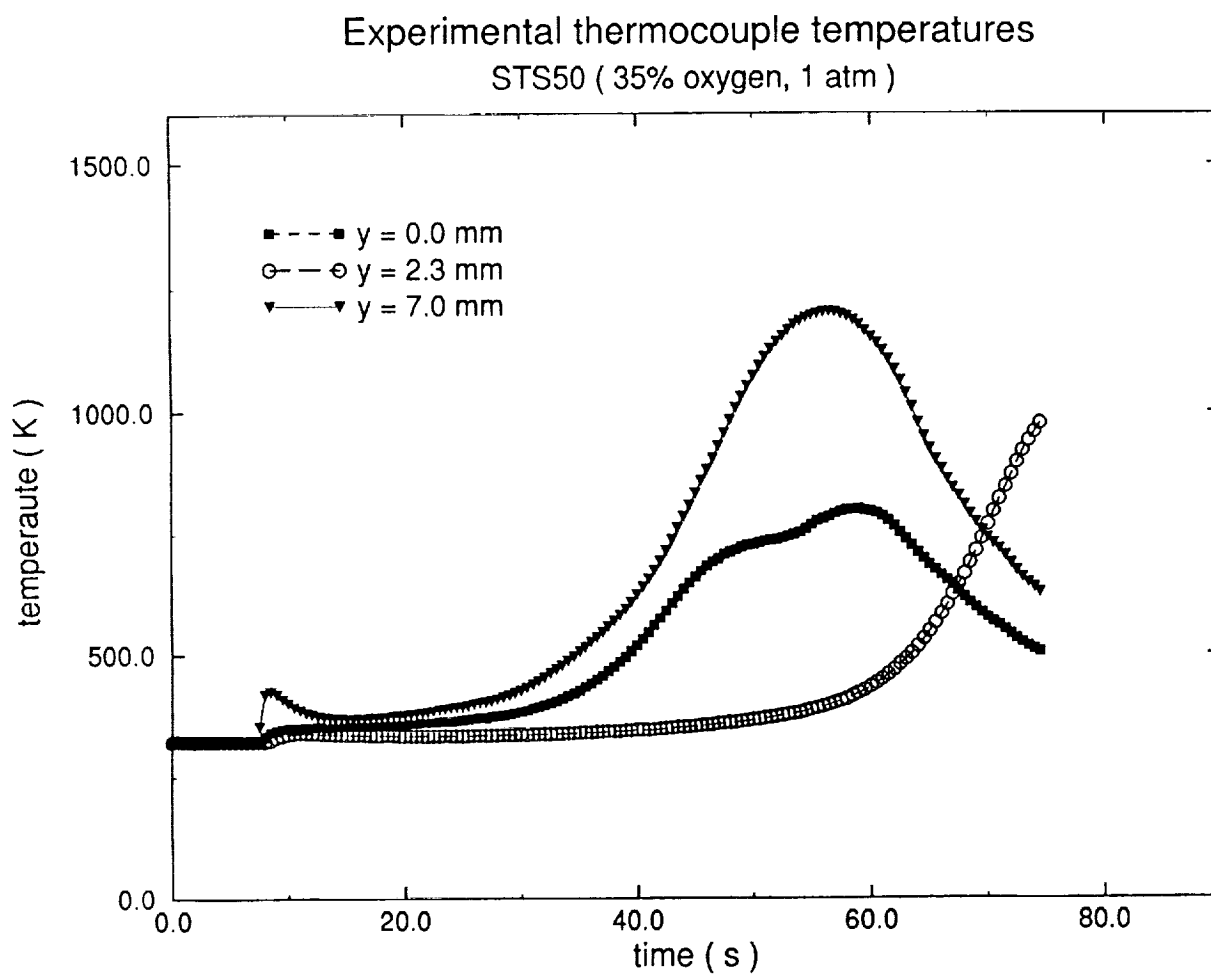


Figure 2 Measured surface and gas-phase temperatures for 35% oxygen, 1.0 atm.

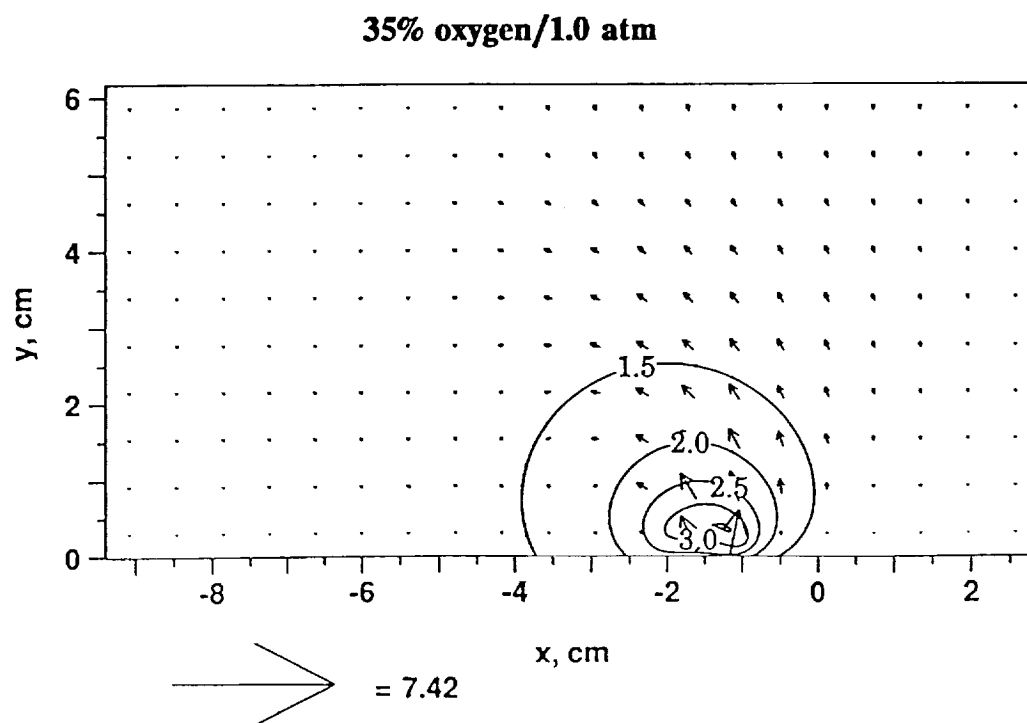
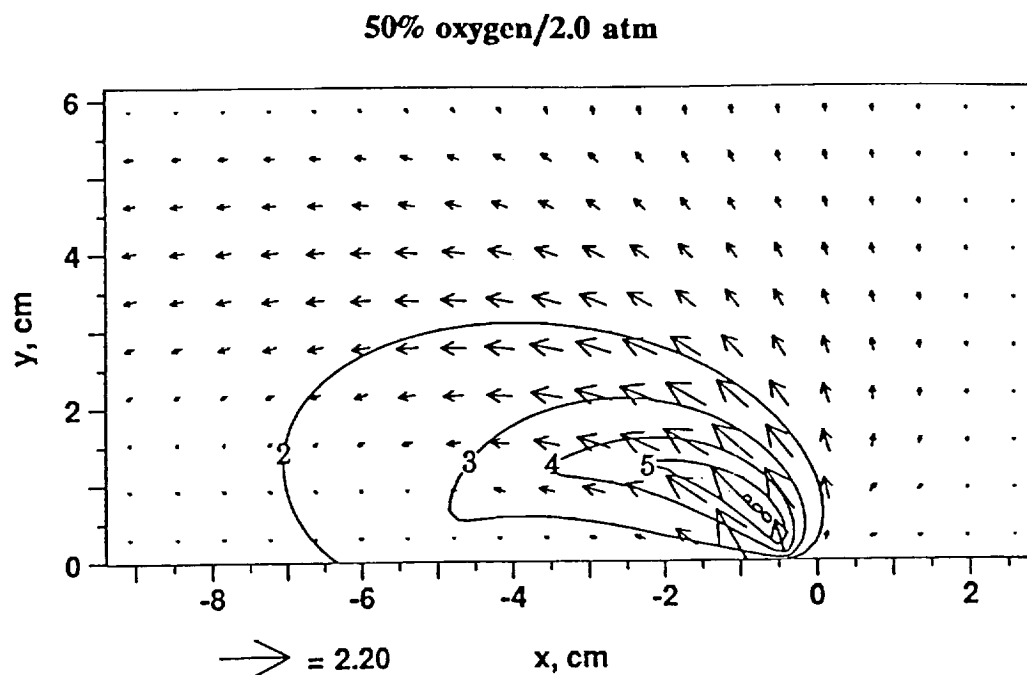


Figure 3 Temperature contours predicted from the steady model with temperatures in the units of the ambient superimposed on the computed vector velocity field relative to the ambient with the vector scale in units of computed spread rate.

Solid-phase thermocouple temperatures

35% oxygen

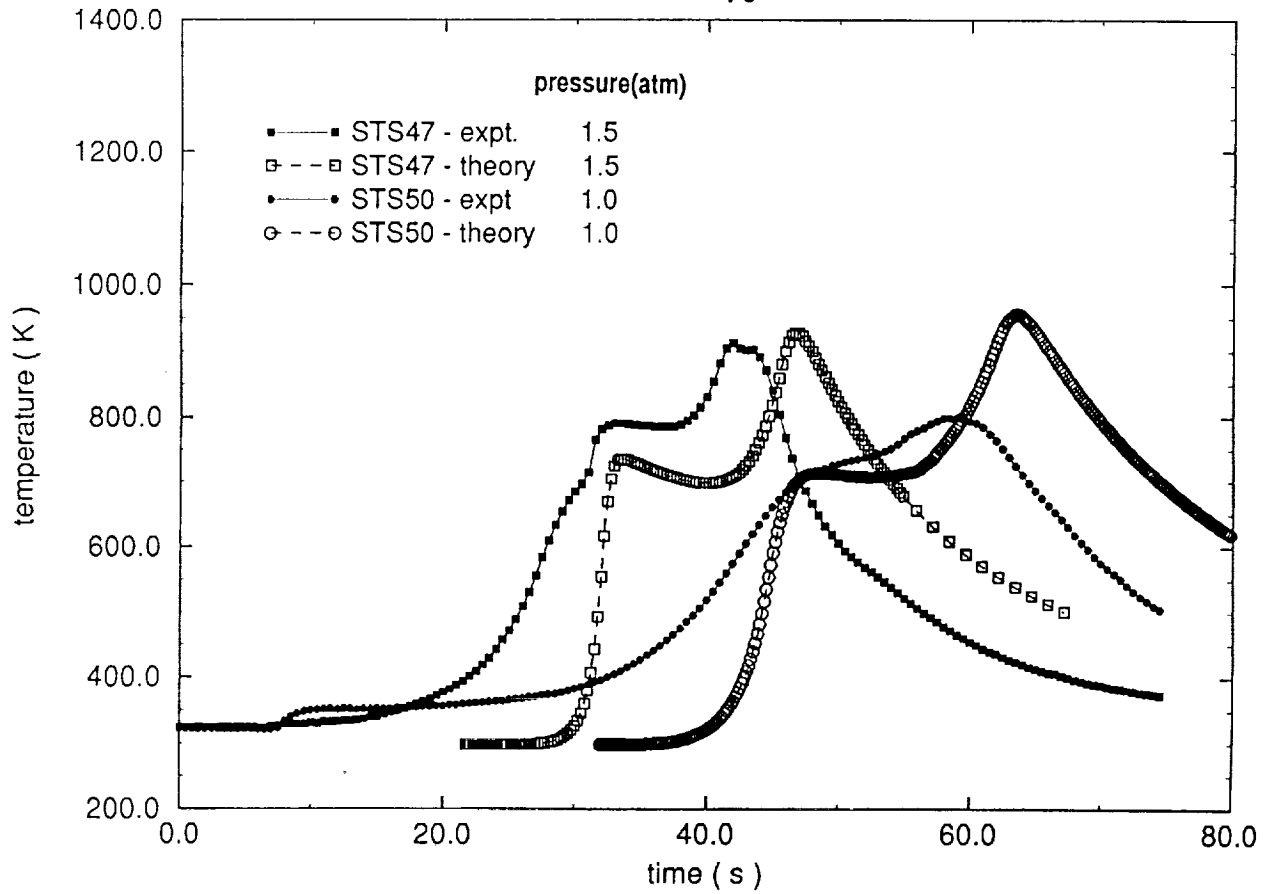


Figure 4 Comparison of measured and predicted surface temperatures from the unsteady model formulation for 35% oxygen.

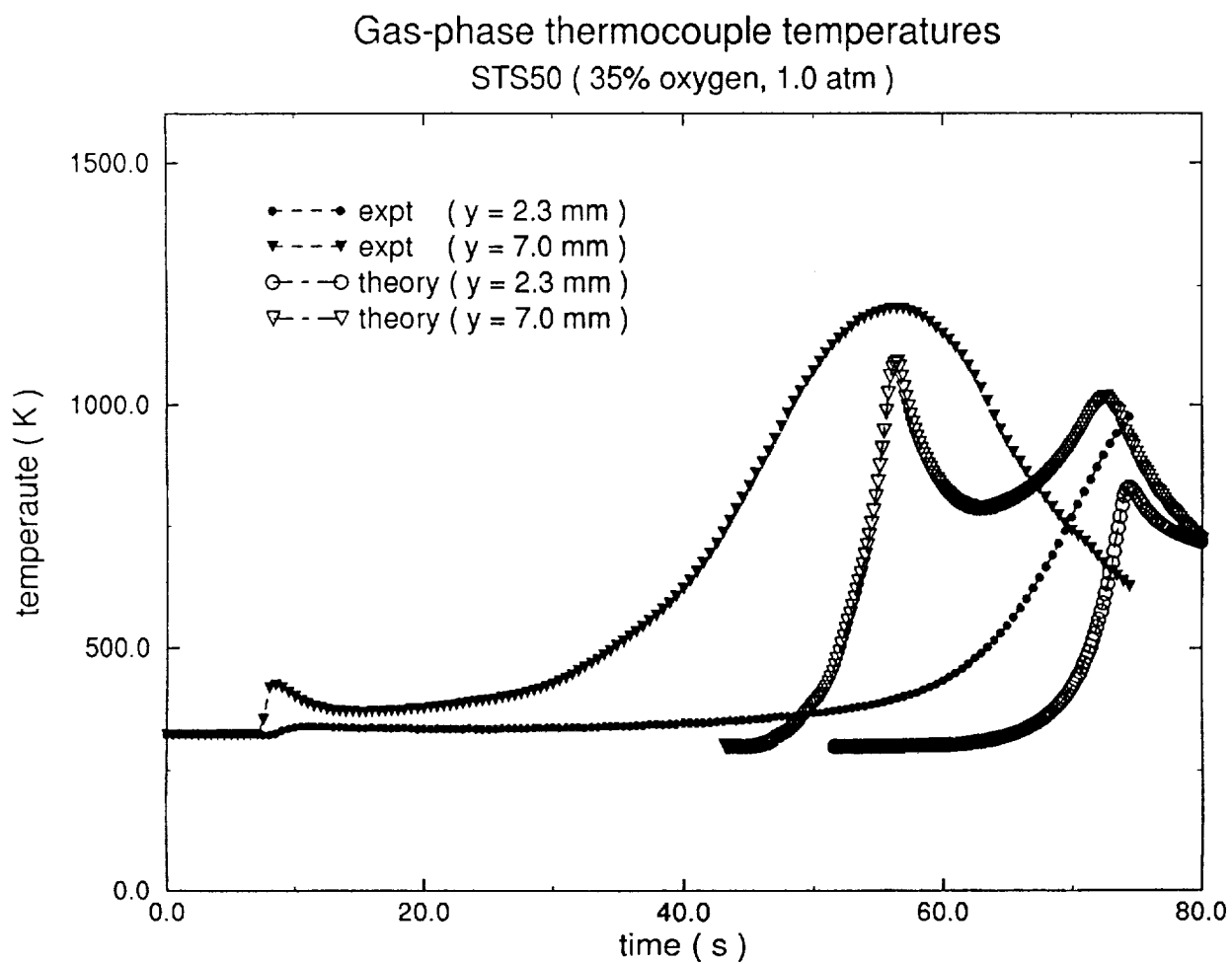


Figure 5 Comparison of measured and predicted gas-phase temperatures from the unsteady model formulation for 35% oxygen.

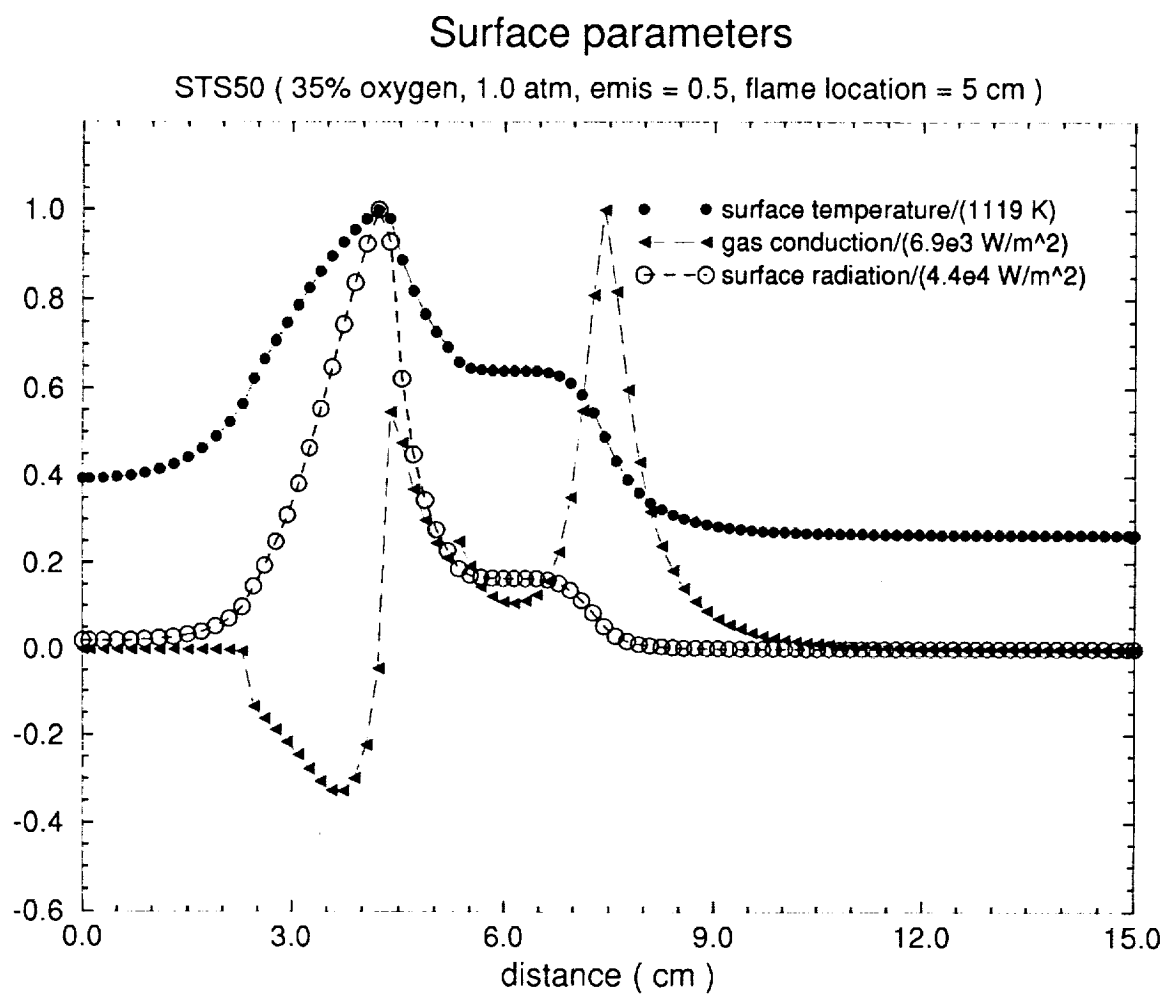


Figure 6 Computed heat fluxes for 35% oxygen, 1.0 atm.

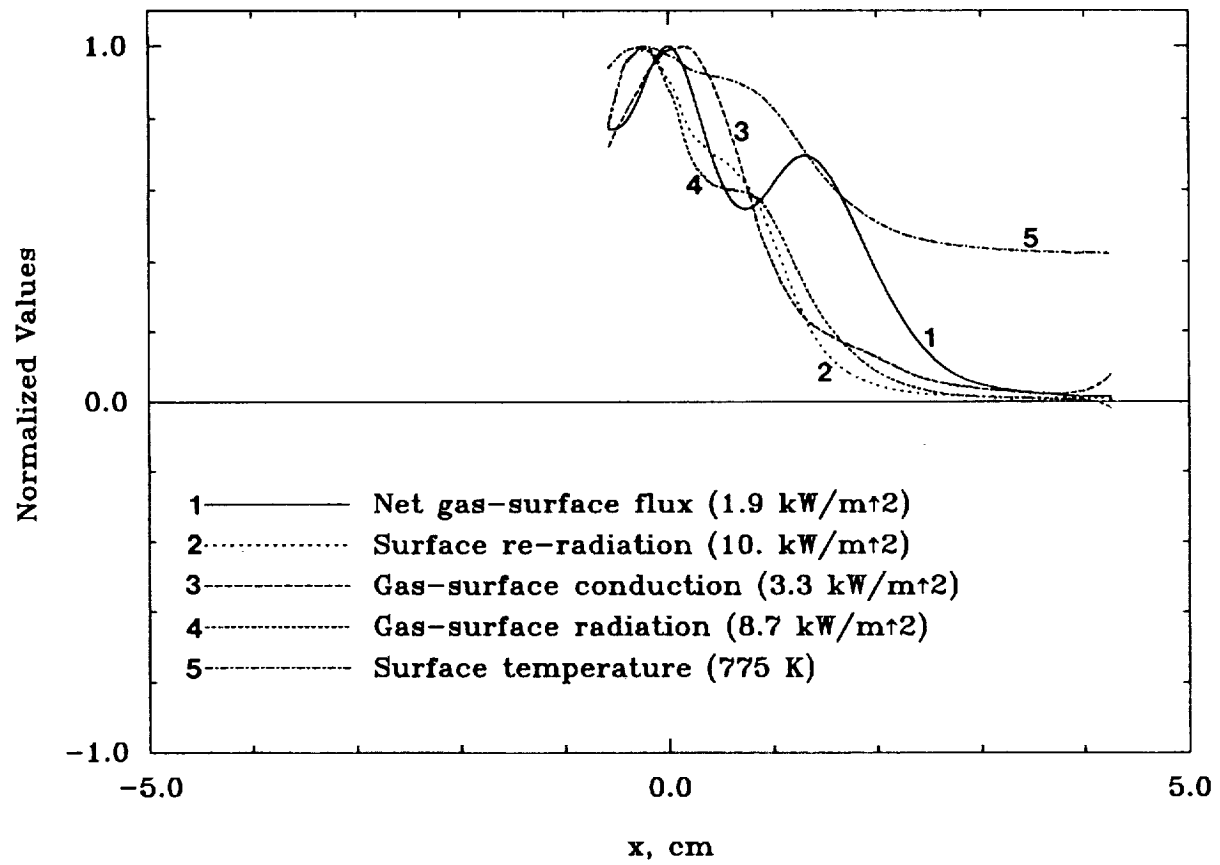


Figure 7 Experimental heat fluxes for 35% oxygen, 1.0 atm.

Surface parameters

STS41 (50% oxygen, 1.5 atm, emis = 0.5, flame location = 5 cm)

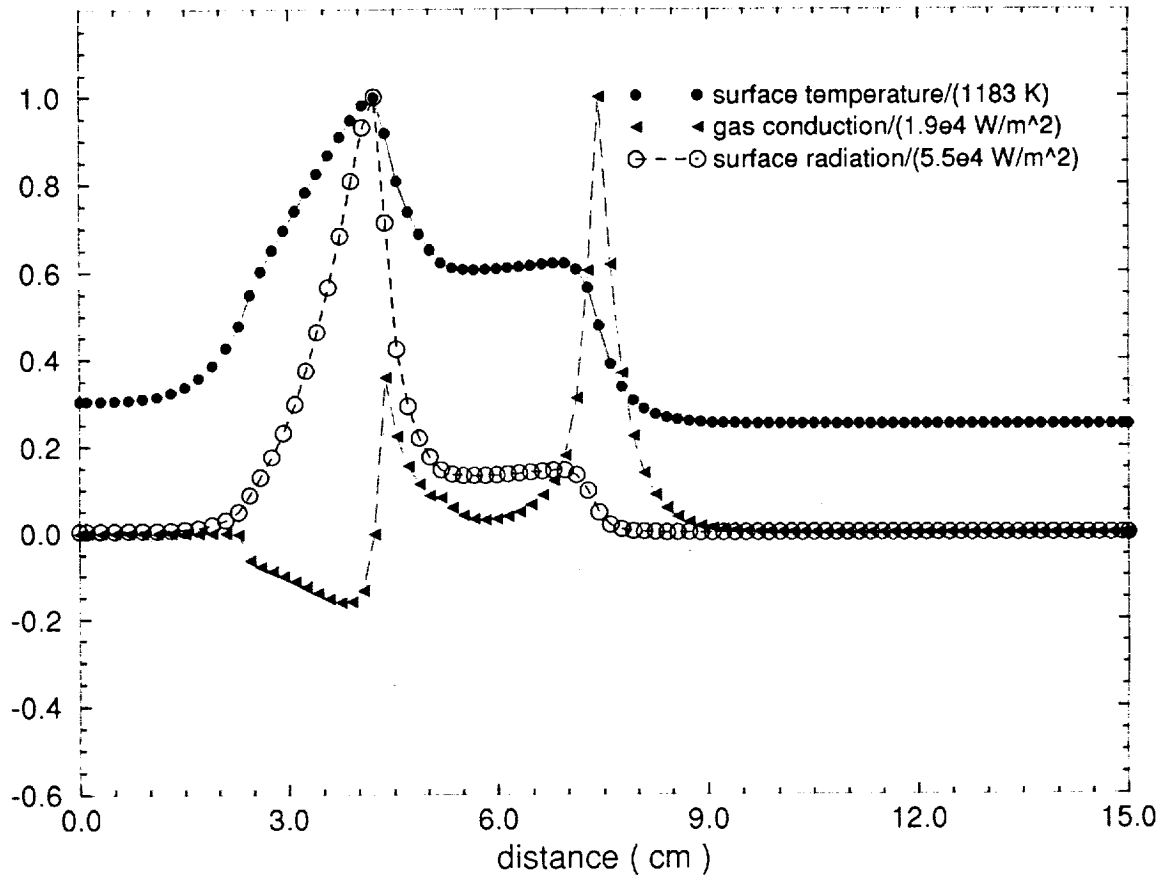


Figure 8 Computed heat fluxes for 50% oxygen, 1.5 atm.

5015

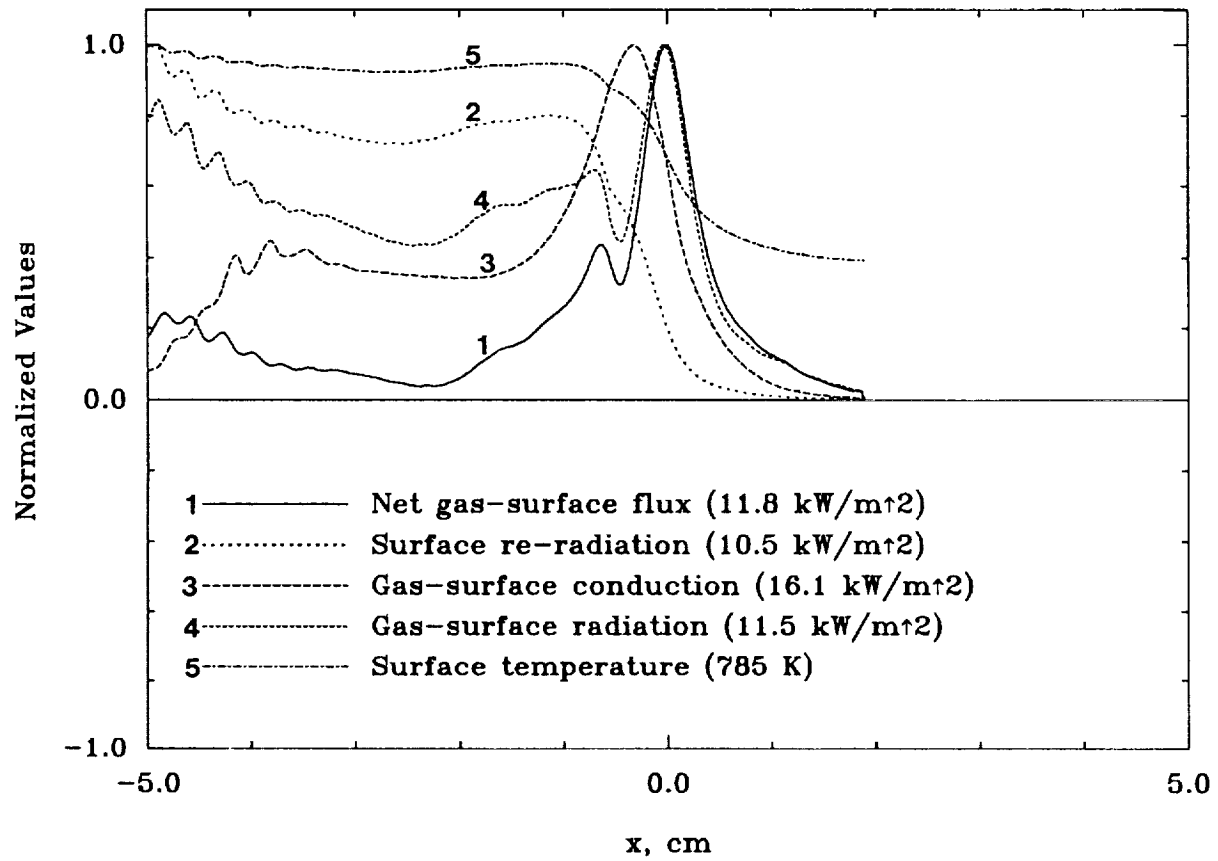


Figure 9 Experimental heat fluxes for 50% oxygen, 1.5 atm.

PRELIMINARY OARE ABSOLUTE ACCELERATION MEASUREMENTS ON STS-50

Robert C. Blanchard*, John Y. Nicholson⁺, and James R. Ritter[^]

*NASA Langley Research Center, Hampton, Virginia 23681-0001

⁺ViGYAN, Inc., Hampton, Virginia 23666-1325

[^]Lockheed Engineering & Sciences Co., Hampton, Virginia 23666-1339

SKIP
P. 5

PREL. ANN
93N 22587

ABSTRACT

Orbital Acceleration Research Experiment (OARE) data on STS-50 have been examined in detail during a 2-day time period. Absolute acceleration levels have been derived at the OARE location, the Orbiter center-of-gravity, and at the STS-50 Spacelab Crystal Growth Facility.

The tri-axial OARE raw acceleration measurements (i.e., telemetered data) during the interval have been filtered using a sliding trimmed mean filter in order to remove large acceleration spikes (e.g., thrusters) and reduce the noise. Twelve OARE measured biases in each acceleration channel during the 2-day interval have been analyzed and applied to the filtered data. Similarly, the *in situ* measured x-axis scale factors in the sensor's most sensitive range were also analyzed and applied to the data. Due to equipment problem(s) on this flight, both y- and z- axis sensitive range scale factors were determined in a separate process (using the OARE maneuver data) and subsequently applied to the data. All known significant low-frequency corrections at the OARE location (i.e., both vertical and horizontal gravity-gradient, and rotational effects) were removed from the filtered data in order to produce the acceleration component at the Orbiter's center-of-gravity, which are the aerodynamic signals along each body axes. Results indicate that there is a force of unknown origin being applied to the Orbiter in addition to the aerodynamic forces. The OARE instrument and all known gravitational and electromagnetic forces have been reexamined, but none produce the observed effect. Thus, it is tentatively concluded that the Orbiter is creating the environment observed.

NOMENCLATURE

A	acceleration
g	gravitational acceleration at sea level ($9,8065 \text{ m/s}^2$)
MET	mission elapsed time (i.e., time from lift-off)
nano-g	$1 \times 10^{-9} \text{ g}$
p,q,r	body axes angular rates
T	temperature
u,v,w	air relative velocity body axes components
V	velocity
V_{air}	air relative velocity
X,Y,Z	sensor axes
X_b, Y_b, Z_b	body axes
α	angle-of-attack
β	side-slip angle
μg	$1 \times 10^{-6} \text{ g}$

Subscripts

o	Orbiter spacecraft coordinates
L	with respect to the center-gravity
rot	rotational

Acronyms

CAS	Calibrated Ancillary System
CGF	Crystal Growth Facility
HiRAP	High Resolution Accelerometer Package
IMU	Inertial Navigation unit
OARE	Orbital Acceleration Research Experiment
STS	Space Transportation System

INTRODUCTION

The orbital acceleration Research Experiment (OARE) consists of a three axis, state-of-the-art accelerometer with an electrostatically suspended proof mass, a full in-flight calibration station, and a microprocessor which is used for in-flight experiment control, processing, and storage of flight data. The experiment system is designed to measure low-frequency (<1 Hz) low-level acceleration (i.e., nano-g sensitivity). An in-depth description of the experiment goals, equipment design characteristics, and capabilities is given in Ref. 1.

The first Shuttle flight of the OARE was June 5, 1991, on the *Columbia* during STS-40. Orbital data were collected for about 3.5 days beginning approximately 5.5 days after launch for this mission. Some equipment problems were noted on the first OARE flight; however, limited results were obtained. These results are given in reference 2.

After the STS-40 flight, the OARE was removed and the problems were isolated and repaired prior to the STS-50 flight. STS-50 is the first flight which employs an operating nano-g sensor coupled with a calibration capability which allows for the measurement of absolute acceleration levels. Over 13 days of orbital data were collected on STS-50. This included over 60 full calibrations sequences which provided both bias and scale factor measurements for 3 axes and 3 ranges. A problem, however, was noted in the most sensitive range for the scale factor measurements on the y -and z-axes. To circumvent the anomaly, OARE maneuvers (three separate rotations about each of the Orbiter's body axes) have been used to provide scale factors for all three axes in the sensor's most sensitive range.

This paper presents the analysis of the OARE data taken during the time period 1^d14^h to 3^d 14^h MET. The analysis of this orbital time segment was selected in order to provide low frequency, low acceleration information for Spacelab furnace experimentation application, e.g. the Crystal Growth Facility. The on-orbit calibration measurements and their applications to the OARE acceleration signals to produce absolute accelerations are discussed. Also presented is the transformation of the data from the OARE location to the Orbiter's center-of-gravity, which provides acceleration data on the drag aerodynamics along each axis.

I. FLIGHT DATA ANALYSIS

A. Orbiter State parameters

Ancillary flight data of the Orbiter's inertial position, velocity vector, and orientation (Aries mean 1950 coordinate system) are received from Goddard Space Flight Center in the form of Calibrated Ancillary System (CAS) tapes. In general, these data give the conditions under which the OARE acceleration measurements were taken. Specifically, the CAS data are interpreted in order to validate the OARE data and to transform the OARE data to other locations (e.g., the center of gravity). The CAS data are transformed into other useful quantities, such as distance from the center of Earth, latitude, longitude, and relative velocity. For relative velocity calculations, it is assumed that the atmosphere is rotating with the Earth. On the CAS tapes, the orientation of the Orbiter is given in quaternions. These are combined with the velocity components to calculate angle of attack, α , and sideslip angle, β . This section gives some of the results from the Orbiter CAS tapes.

Figure 1 shows the relative velocity and the altitude variations as a function of MET in hours. The altitude is referenced to a spherical Earth with a radius of 6356.766 km. As seen, the orbit is very

circular; a difference of only 9 km exists between perigee and apogee. The altitude range is about 325 km to 316 km and the orbit is slightly changing with time. The expected mean aerodynamic drag is very small and the 90 min, variation due to the slightly elliptical orbit is even smaller (e.g., using the 1976 US standard atmosphere³, the acceleration signal is estimated at about 275 ng with a variation of ± 25 nano-g).

Based upon the CAS data, the Orbiter is oriented with the payload bay doors toward the velocity vector with the right wing tilted about 12° into the velocity vector (i.e., forward of a line perpendicular to the orbital plane). The orientation is shown in Fig. 2 where the engines are pointed toward Earth and the payload doors are open. The insert graph in Fig 2 shows the α and β flight data for entire period. Both angles are tightly held to $\pm 1/2$ deg centered around $\alpha = -90^\circ$ and $\beta = 12^\circ$. For completeness, the definitions⁴ of α and β are as follows:

$$\alpha = \tan^{-1}(w/u) \text{ and}$$

$$\beta = \sin^{-1}(v/V_{\text{air}}),$$

where u , v , and w are body axes velocity components of V_{air} and V_{air} is the magnitude.

In this orientation, it is anticipated that the majority of the aerodynamic effect is along the positive z-body axis. The y-body axis acceleration should be negative and very small due to an aerodynamic force produced on the right side of the Orbiter facing into the velocity vector. The x-body axis acceleration signal should be positive, almost entirely due to gravity-gradient and rotational effects. Figure 2 also shows the body axis coordinate system.

Figure 3 shows the Orbiter's three body rates during the entire period. Clearly, roll rate, p (the angular rate about the x-body axis) is on the average nearly zero. If the Orbiter y-body axis were held perpendicular to the orbital plane, the pitch rate, q , (the angular rate about the y axis) would be equivalent to rotating the Orbiter 360° over the orbital period of 90 minutes (i.e., 0.067 deg/s). The y axis is not quite perpendicular to the orbital plane so that this rate component is slightly reduced. The yaw rate, r , (the angular rate about the z axis) shows an approximate value of 0.014 deg/s due to the 12° offset mentioned earlier.

B. In-flight calibrations

The success of making low frequency, low amplitude acceleration measurements at orbital altitudes relies heavily on providing reliable calibration factors. The OARE plays a unique role in the technological development of systems for making these calibration measurements. It has a complete calibration station providing both *in situ* bias and scale factor measurements. This section of the report discusses the instrument operating conditions and shows the calibration data taken during the interval.

The instrument was programmed to perform a calibration sequence approximately every 4.75 hours. The calibration sequence includes up to nine separate bias calibrations (three axes, three ranges) and up to six scale factor calibrations (two table rate/axis, with y and z axes scaled simultaneously). A bias calibration consists of collecting 50 s of data in one position, rotating the sensor 180°, and then collecting data for another 50 s period. The sum of the average of each interval is twice the bias, while the difference is twice the average input signal. A scale factor calibration consists of rotating the sensor at a pre-programmed rate and measuring the acceleration difference between the sensor at rate and the average output at rest. This difference is scaled to the known centripetal acceleration which is a function of the square of the rate (which is measured) and the location of the sensor on the table (which is known). Two table rates are used for each sensor range for linearity checks.

Figure 4 shows the temperature measurements from two thermocouples, one inside the sensor package and one mounted on the base, adjacent to the rotary table surface. Throughout the entire period, the temperature varied by about 4°C, getting cooler as the mission progressed. It is interesting to observe the diurnal variation of about 1°C. This type of variation has the potential to seriously limit the interpretation of pendulous type accelerometer drag variations because typical bias temperature sensitivity coefficients are 20 to 60 $\mu\text{g}/^\circ\text{C}$ for these instruments. That is, for these accelerometers, it is difficult to separate diurnal drag variations from sensor temperature effects since both effects are in phase. It has been demonstrated that ground based calibrations of these instruments in a 1-g environment produce significant errors when applied to the micro-gravity environment produce significant errors when applied to the micro-gravity environment encountered on orbit.⁵ There are two important reasons why OARE is not seriously affected by this phenomenon. First, *in situ* calibrations are made and thus no extrapolations to space are necessary. Secondly, the OARE bias temperature sensitivity coefficients are very small, typically much less than 1 $\mu\text{g}/^\circ\text{C}$.

Figures 5, 6, and 7 show the results of the x, y, and z body axes bias calibrations, respectively. Included in each figure is the temperature at each calibration point. In addition, each time a bias is performed, the true (i.e., bias independent) signal is simultaneously measured and is shown along with the bias on each graph, labeled "signal". From the graphs, it is clear that the bias correction is only a few μg except for the y axis which is about 7 μg . This is within OARE design specifications. The x axis has the largest temperature sensitivity, about 0.2 $\mu\text{g}/^\circ\text{C}$, while both y and z are an order of magnitude smaller. The discrete signal measurements on each axis give a 12 point sample of the expected Orbiter residual acceleration environment, except for scale factor adjustments. Clearly, the x axis has a relatively large, almost constant 1.0 μg signal, while y axis is less than .5 μg and z axis varies about 0.8 μg . This is useful information for checking the adjustments to the measured signals which are discussed later.

The scale factors for the x-axis in its most sensitive range were successfully measured *in situ* using the two programmed calibration table rates. The low and high table rates produce calibration accelerations of approximately 20 μg and 45 μg , respectively. Figure 8 shows the scale factor results along with the instrument temperature as a function of time. The scale factor temperature sensitivity for this axis, in this temperature interval is about 0.3%/°C. As noted earlier, the *in situ* scale factor measurements for the y- and z-axes in the most sensitive range were unsuccessful. These scale factors were determined using data taken during the OARE data to solve for the scale factors on all three axes. Table 1 summarizes the scale factor results.

The *in situ*-axis scale factor compares moderately well with the one derived from the maneuvers. Several facts are worth mentioning about the possible source for the differences. First, the OARE maneuver occurred late in the mission (on day 12 MET) when the instrument was at a different temperature (cooler). Second, typically each maneuver involves rotating the spacecraft 360°. Rate motion is obtained from gyro processing during the scale factor extraction process. The gyros require calibration factors which introduce errors,

II. OARE GROUND PROCESSING

OARE collects tri-axial data at the rate of 10 samples/s. The data are filtered thorough an analog filter and a 6 pole Bessel filter with a cutoff frequency of about 1 Hz. This raw data are too noisy for use in detailed characterization of low frequency analysis.

By design, the raw data are telemetered to ground stations and simultaneously processed on-board by the OARE computer using a 'trimmed-mean' filter. Briefly, this filter consists of ordering a window of data (for STS-50, the window size was set at 500 samples) from low to high values. Then, a 'q statistic' is calculated which gives a measure of outlier content. From this, a percentage of the 'tails' of the data is eliminated. The remainder of the data are averaged and the window slides in time (for STS-50, 25 seconds was chosen). Examination of this data revealed that it was still slightly noisy for the purpose of this report. In addition, a check was required to determine whether the on-board computer was handling the data correctly. Thus, it was decided to ground process the raw telemetered data in the same manner as the on-board computer, except vary the window size. However, after the study, it was evident that the flight data processing algorithm performed as planned.

A. OARE Location Environment

Figure 9 shows the OARE measured x, y, and z acceleration levels in the Orbiter's body axes system at the OARE location. The data in this figure are the OARE 10 samples/sec telemetered raw (unprocessed) data which have been averaged using a trimmed-mean technique with a window of 200 sec sliding at 25 sec intervals. This digital filter essentially limits frequency observability to less than

about 0.0025 Hz. However, this introduces no problems since this frequency is much larger than those associated with orbital phenomena of interest. The data have been corrected with the OARE biases and scale factors.

The x-axis appears to produce the largest signal of about $1 \mu g$ with an oscillatory wave of period 26 hours. The y-axis signal is positive and smaller than the x-axis (about $0.6 \mu g$), and also has an oscillatory signal of about 26 hours which is 180° out of phase with the x-axis data.

B. Center of Gravity Environment

The location of the OARE sensor in body axes coordinates relative to the Orbiter's center-of-gravity is $X_b = -1.536$ m, $Y_b = -0.0234$ m, $Z_b = 1.435$ m. Based upon this lever arm and the Orbiter orientation data discussed earlier, the magnitude of the major adjustments, namely, gravity-gradient and rotational effects, is shown in Fig. 10. The gravity-gradient effect includes both vertical and horizontal displacements from the Orbiter center-of-gravity. Clearly, the largest correction is on the x axis, about $0.65 \mu g$, with components from gravity-gradient and rotational effects. The total of the y axis corrections is an order of magnitude smaller and its source is mostly rotational effects. The net correction for the z axis is practically zero due to the cancellation of the gravity-gradient effects with the rotational contributions. Applying these adjustments to the data shown in Fig 9 should theoretically give the accelerations at the Orbiter center-of-gravity which are the drag measurements. The results are shown on fig. 11. Clearly, the value of the residual acceleration along the x axis is much too large to be attributable to the x axis, the aerodynamics should be very nearly zero. Further, the signal also has an obvious 26 hours oscillation. The z axis also has this oscillation at about the same frequency. The z axis data contain the 90 min drag oscillation similar to that observed during STS-40². The y axis appears about as expected: namely, a small slightly negative acceleration which is mainly attributable to aerodynamics.

Several physical phenomena associated with a 24-hour period have been investigated, such as oblate Earth, geomagnetically induced forces, solar radiation pressure, etc. However, none of the considerations to date have produced the proper amplitude and frequency. Thus, a possible alternative is that the Orbiter itself is producing the environment being measured by the OARE sensor. Of course, this requires further investigations.

C. CGF Location Environment

The accelerations caused by this force of unknown origin and the aerodynamic forces are given in Fig. 11. This represents the external forces exerted on the Orbiter at the center-of-gravity. The corresponding accelerations at any other location can be obtained by adding to these measurements the predictions due to gravity-gradient and rotational effects at this location.

The location of the Crystal Growth Facility (CGF) melt location,⁶ in Orbiter Project spacecraft coordinates, is $x_0 = 1086.00$ in., $y_0 = -44.39$ in., $z_0 = 395.45$ in. This corresponds to a lever arm about the center-of-gravity of $X_1 = 0.173$ m, $Y_1 = 1.117$ m, $Z_1 = -0.537$ m. Using this lever arm with the orientation and Orbiter rotation rate data from the CAS tapes, the corrections to the CGF location have been calculated and the results are shown in Fig. 12. Shown are the individual is about $-0.16 \mu\text{g}$ in the y axis due to gravity-gradient horizontal displacement effects. Both x and z axis corrections are fairly small, namely about -0.07 and $-0.035 \mu\text{g}$, respectively.

Figure 13 shows the final results of the low frequency acceleration environment at the CGF melt location. This is obtained by applying the results shown in Fig. 12 to Fig. 11. The acceleration along the x-axis ($\sim 0.5 \mu\text{g}$) is dominated by the acceleration created by the unknown force, possibly the Orbiter itself. The expected acceleration due to drag in this axis is much smaller, approximately an order of magnitude less. The acceleration along the y-axis is slightly negative ($\sim 0.2 \mu\text{g}$) due to aerodynamics and horizontal displacement effects. The z-axis acceleration shows the diurnal atmospheric effect. This effect is seen in Fig. 13 as the higher frequency variation within the 26 hour variation caused by the component of the unknown force in the z direction.

III. ERROR ESTIMATION

The largest and most important error source along all three axes would be from incorrectly estimating the bias. Consequently, care has been taken with this quantity throughout the analysis. For this study, a simple straight line was fit through the measured bias values. The average value and slope will cause no consistent error greater than $0.05 - 0.07 \mu\text{g}$. (it's entirely possible that a given bias could be in error more than this, but it is likely that the biases on either side would not.) In addition, uncertainties in scale factors, knowledge of the center-of-gravity, and rotation rates contribute to errors. These errors could be cumulative, but most probably are not. Estimates of their error contributions are listed in Table 2.

At this time, there remain two unresolved questions from the analysis. First, what is the source of the unpredictable acceleration in the x direction? The x axis signal offset is clearly too large to be attributable to aerodynamics based upon an assessment using data from Ref. 7. In order for gravity-gradient and rotational effects to generate the unforeseen acceleration, the center-of-gravity would have to move about 40 in., which is unrealistic. However, it would take only a few ounces of force exerted on the Orbiter to produce this effect (since $1 \text{ oz.} = 0.26 \mu\text{g}$). A component of this force has to be exerted in the positive x direction, which would occur with a gas leak in the opposite, i.e., negative x direction.

The second question (which is most likely related to the first) is: What is the cause of the 26 hour oscillations seen in both the x- and z- axes? This oscillation in the z direction would certainly require that

a gas leak has a component in the z direction. Since the phase of the oscillation in the z axis 180° with respect to the x axis, the z force component has to be exerted on the Orbiter from its underside. Therefore, the leak would be directed downward as well as backward from the Orbiter. Of course, if there is a continuous leak in the plane of the orbit, then the orbit itself would undergo a slight change. There is a slight change in orbit conditions (see Fig. 2). But, at this time, it is not known if the observed change in orbit is due to a leak, a result of cumulative attitude-keeping jet firings, or simply natural phenomena such as tidal effects, etc.

Rechecking the data, its processing, and calibration revealed no errors. The bias values for both x- and z-axes show no anomalies. Also, the signals calculated concurrently with the biases are in good agreement with the data once the data signals are adjusted for bias. Although no definitive explanation exists at the present time, all evidence indicates that both effects are real and should be included in the acceleration environment.

SUMMARY

The OARE data on STS-50 during the time period 1d 14h to 3d 14h MET (38h to 86h MET) have been examined in detail and absolute acceleration levels have been derived at the location of the OARE, the Orbiter center-gravity, and the STS-50 Spacelab at the location of the OARE, the Orbiter center-of-gravity, and the STS-50 Spacelab Crystal Growth Facility.

The tri-axial OARE raw acceleration measurements (i.e., telemetered data) during the interval have been filtered using a 2000 point trimmed mean filter moved every 250 points (OARE sample rate is 10 samples/s). This process removes large acceleration spikes due to thrusters, etc. and reduces the noise. The 10 OARE measured biases in each channel during the 2d interval were analyzed and applied to the filtered data. Similarly, the x-axis scale factors were also analyzed and applied to the data. Both y- and z- axis scale factors were determined in a separate process (using the OARE maneuver data) and subsequently applied to the data. All known significant corrections at the OARE location (i/e., gravity - gradient effects from both vertical and horizontal displacements, and rotational effects) were removed from the filtered data in order to produce the aerodynamic signals along the 3 body axes. However, the results indicate that there is a force of unknown origin being applied to the Orbiter in addition to the aerodynamic forces. The force characteristics are such that they produce a cyclic acceleration with a period of ~26 hours and an amplitude of 0.1 to 0.2 μg residing on top of a magnitude of about 0.5 μg , in the plane of the orbit. Upon re-examination of the OARE instrument, there is no evidence that the equipment is malfunctioning. Further, all known gravitational and electromagnetic forces have been reexamined and none produce the observed effect. Thus, it is tentatively concluded that the Orbiter is

creating the environment observed (e.g., an oscillatory gas leak of a few ounces of force in the aft direction could produce the effect). Obviously, this situation requires further investigation.

The aerodynamics data (with the unknown force are mapped to the Crystal Growth Facility (CGF) location by adding the adjustments to the measurements for gravity-gradient and rotational effects. The enclosed Fig. 13 shows the final results. The acceleration along the x-axes ($\sim 0.5 \mu g$) is dominated by the acceleration created by the unknown force, possibly the Orbiter itself. The acceleration along the y-axis is slightly negative ($\sim 0.2 \mu g$) mostly due to aerodynamics and gravity-gradient horizontal displacement effects. The z-axis acceleration shows the diurnal atmospheric effect, about $0.6 \mu g$ s. This effect is observed in conjunction with the 26-hour oscillation caused by the z-component of the unknown force.

REFERENCES

1. Blanchard, R. C., Hendrix, M. K., Fox, J. C. Thomas, D. J., and Nicholson, J. Y., "The Orbital Acceleration Research Experiment," *Journal of Spacecraft and Rockets*, Vol. 24, No. 6, Nov-Dec. 1987, pp. 504-511.
2. Blanchard, R. C., Nivholdon, J. Y., and Ritter, J. R., "STS-40 Orbital Acceleration Research Experiments Flight Results During a Typical Sleep Period." *Microgravity Science and Technology* Vol. 2, 1992, pp. 86-93.
3. U.S. Standard Atmosphere, 1976, NOAA, NASA. USAF, Oct. 1976.
4. Etkin, Bernard, *Dynamics of Atmospheric flight*, John Wiley and Sons, Inc., New York, 1972, p. 114.
5. Blanchard, R. C., Larman, K. T., and Moats, C.D., "Flight Calibration Assessment of HiRAP Accelerometer Data," AIAA paper 93-0836, January 1993.
6. C. Baugher, MSFC, *Private communications*.
7. Aerodynamics Design Data Book-Vol. I: Orbiter Vehicle, NASA CR-160386, 1978.

Table 1

AVG. SCALE FACTORS*		
axis	in situ	maneuvers
x	1.03	0.93
y	—	1.06
z	—	0.96

*actual SF($\mu\text{g}/\text{count}$)/design SF($\mu\text{g}/\text{count}$)

Table 2

ACCELERATION ERRORS			
Quantity	x_b (μg)	y_b (μg)	z_b (μg)
scale factor	.030	.020	.060
center-of-gravity	.035	<.020	.022
rotation rates	.070	.020	.060

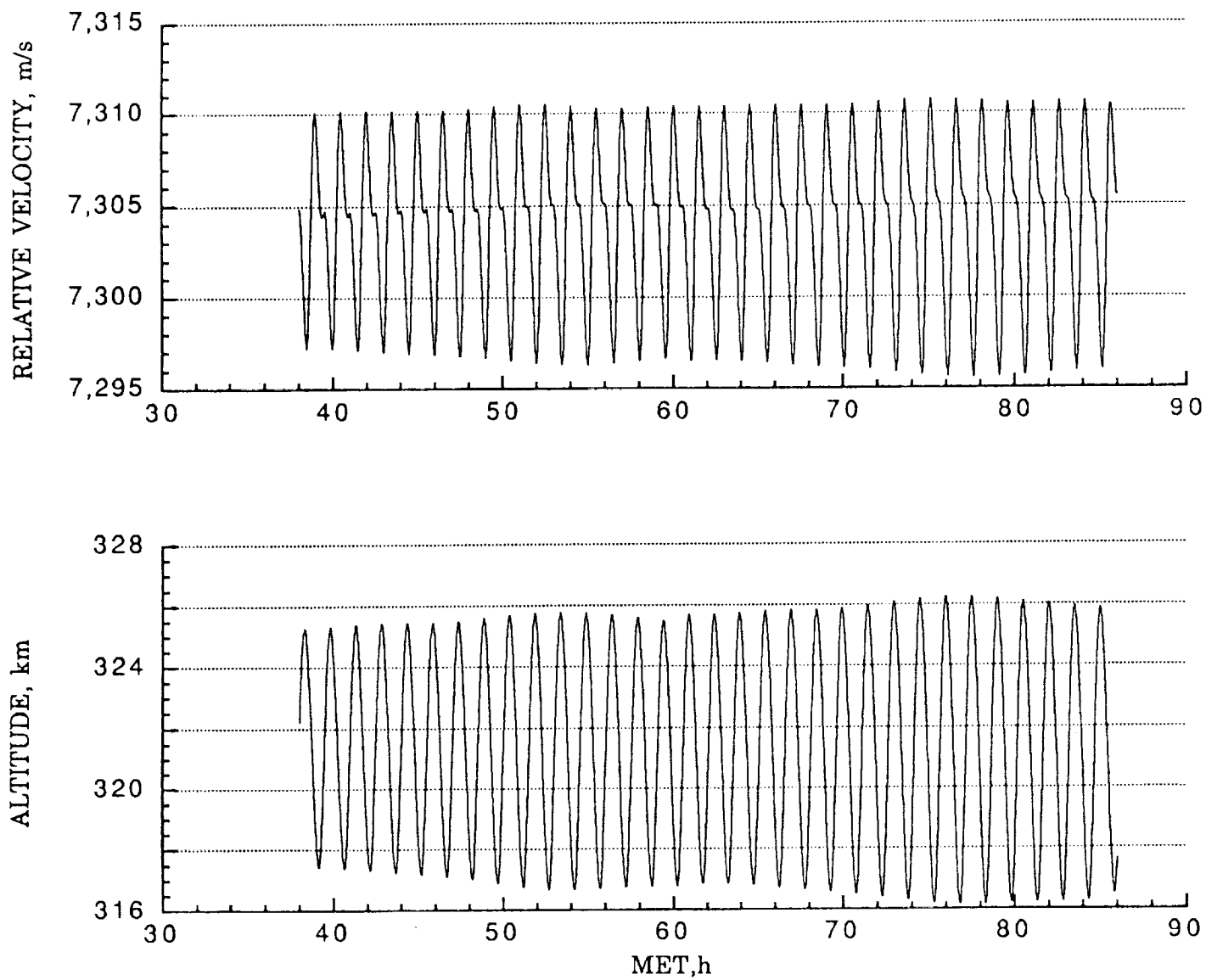


Figure 1 Orbiter relative velocity and altitude time history.

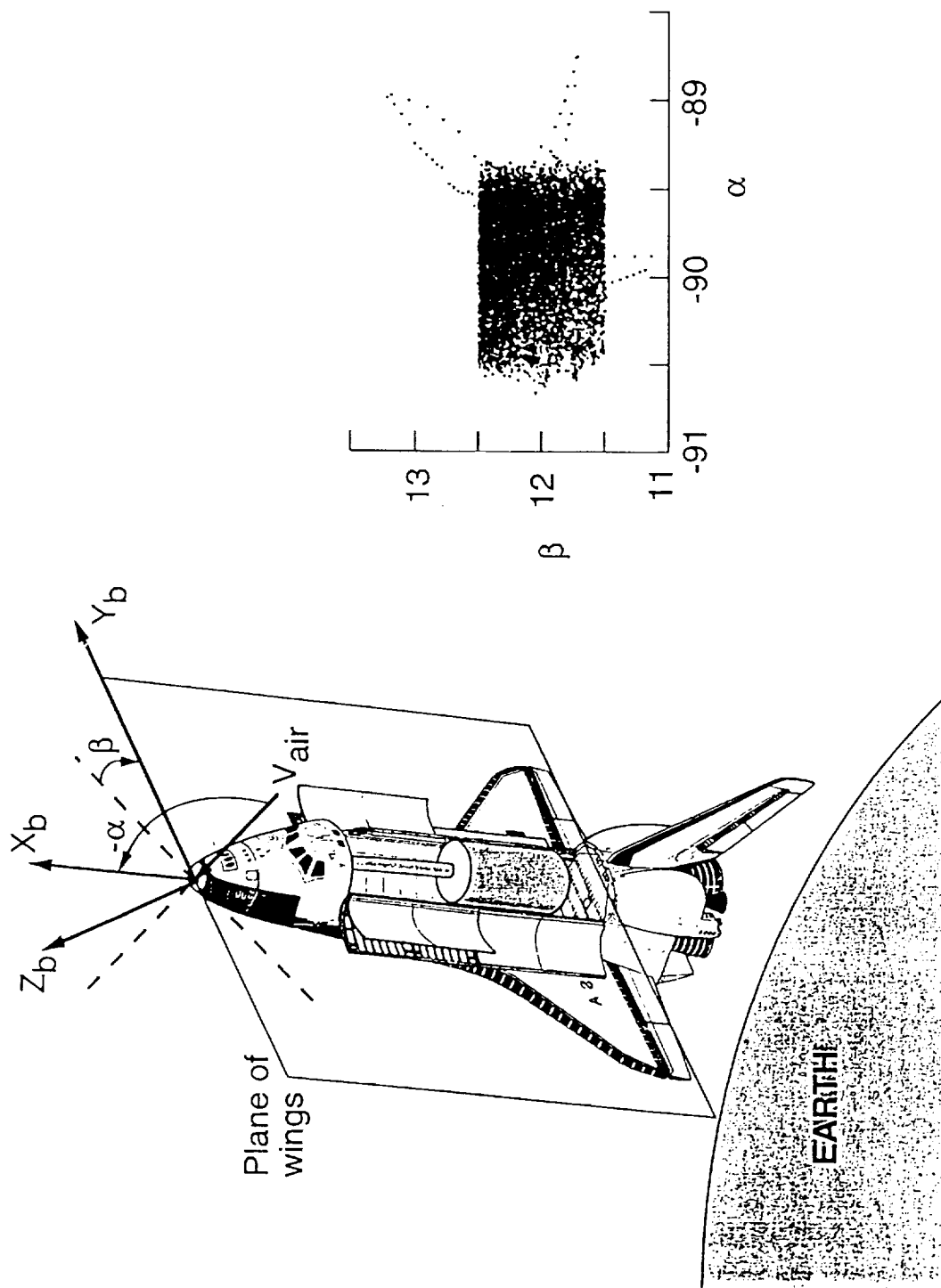


Figure 2 Orbiter orientation and measurements.

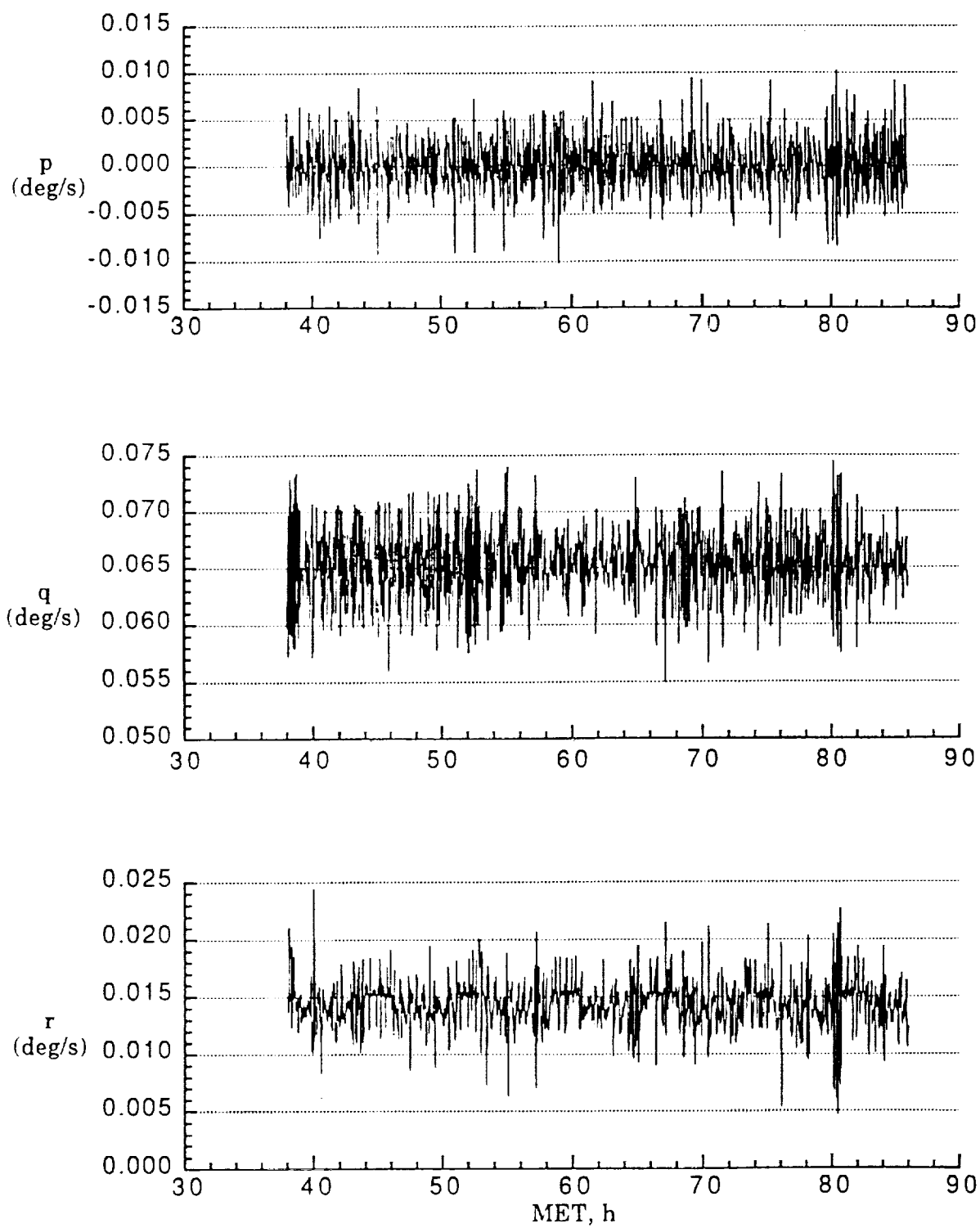


Figure 3 Orbiter angular body rates.

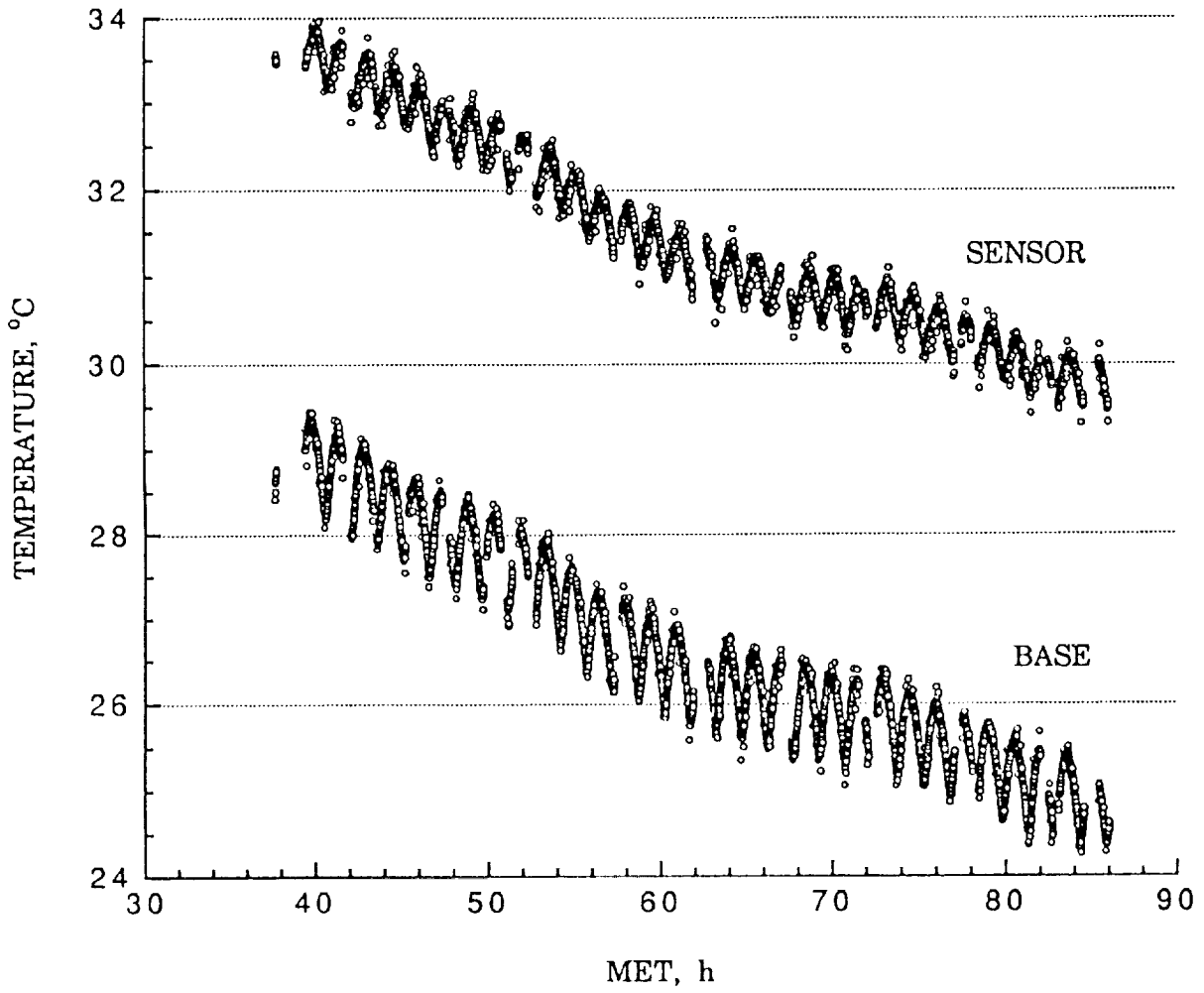


Figure 4 OARE Sensor temperature measurements.

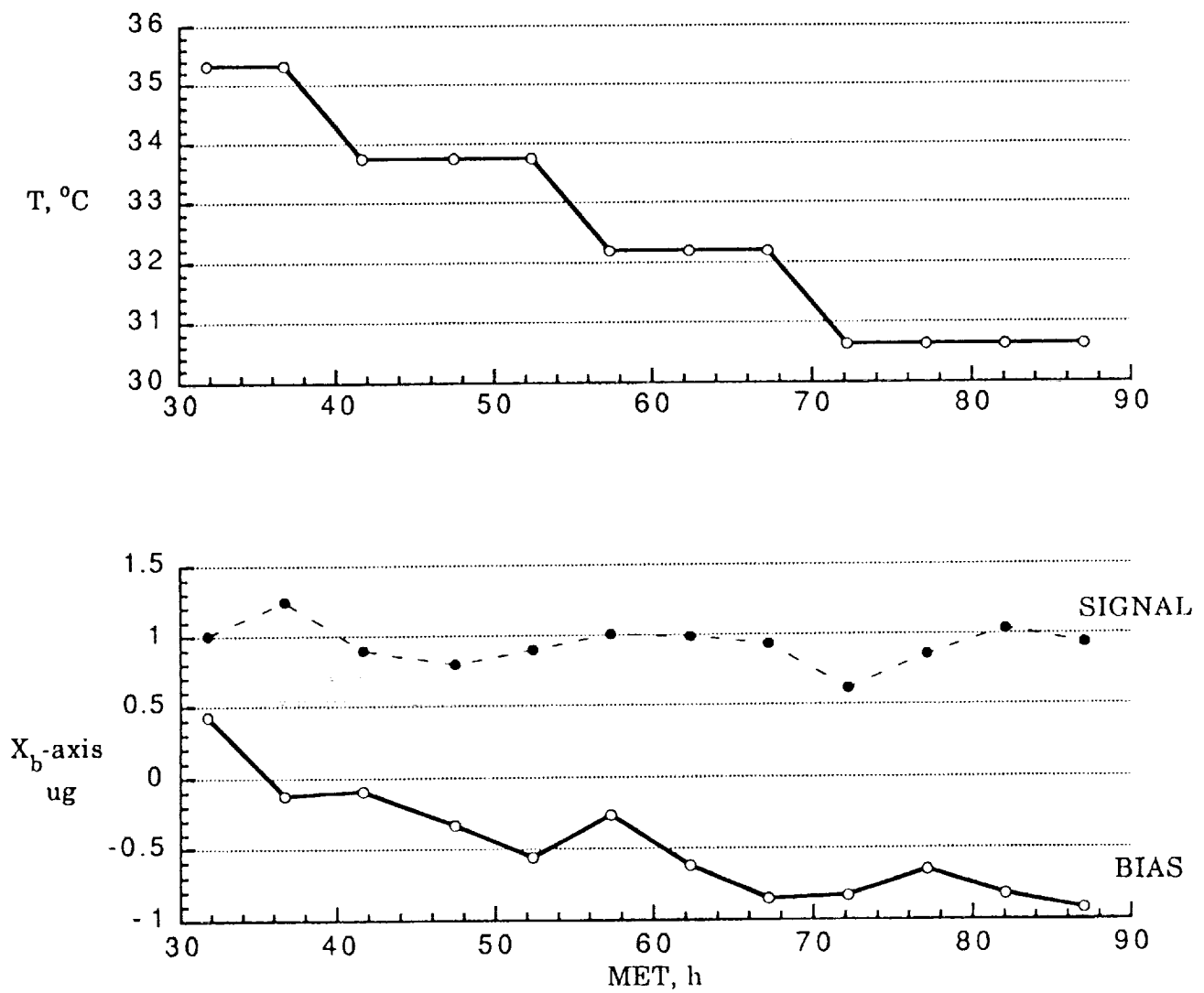


Figure 5 X-body axis sensor temperature, bias, and signal measurements.

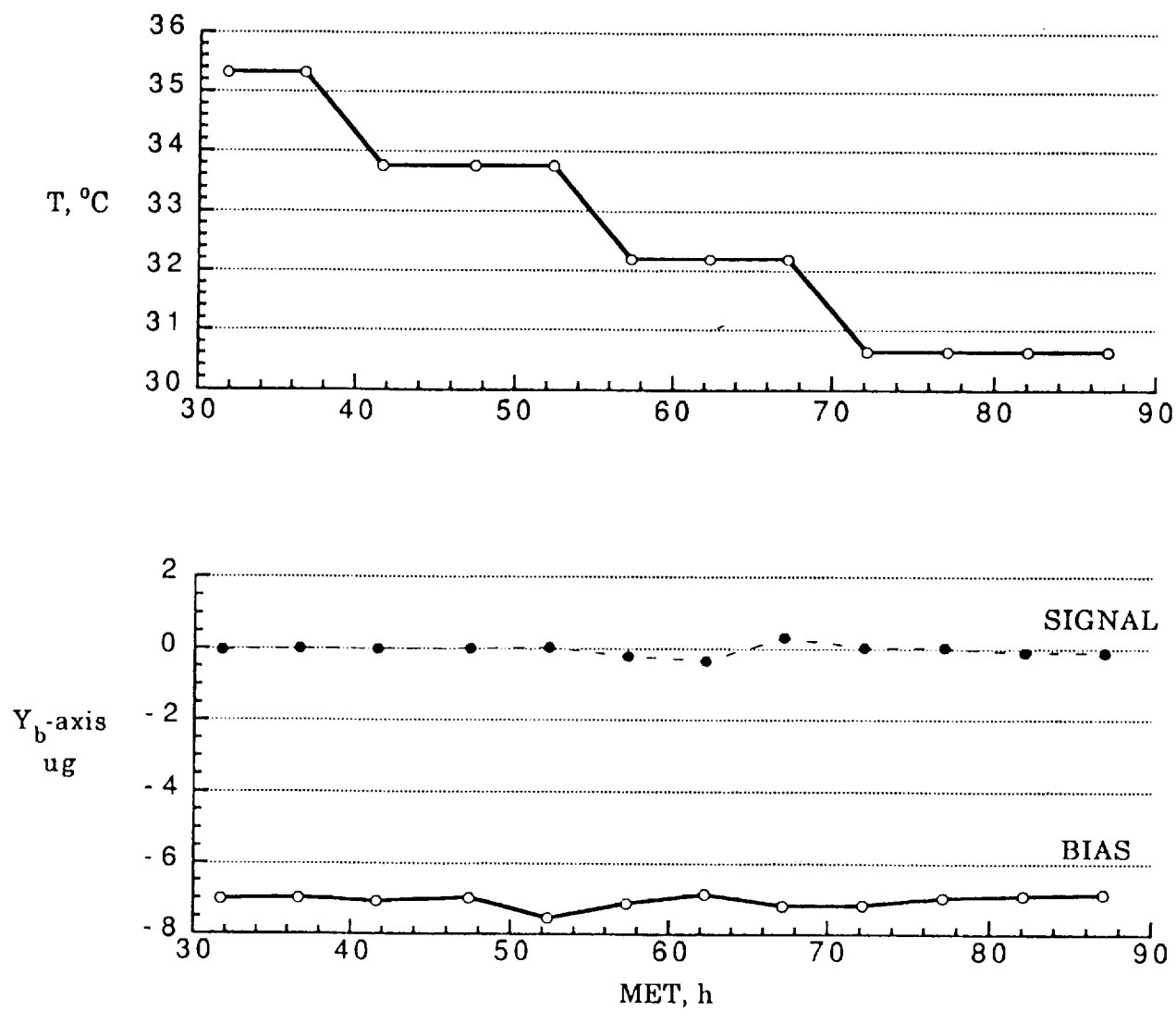


Figure 6 Y body axis sensor temperature, bias, and signal measurements.

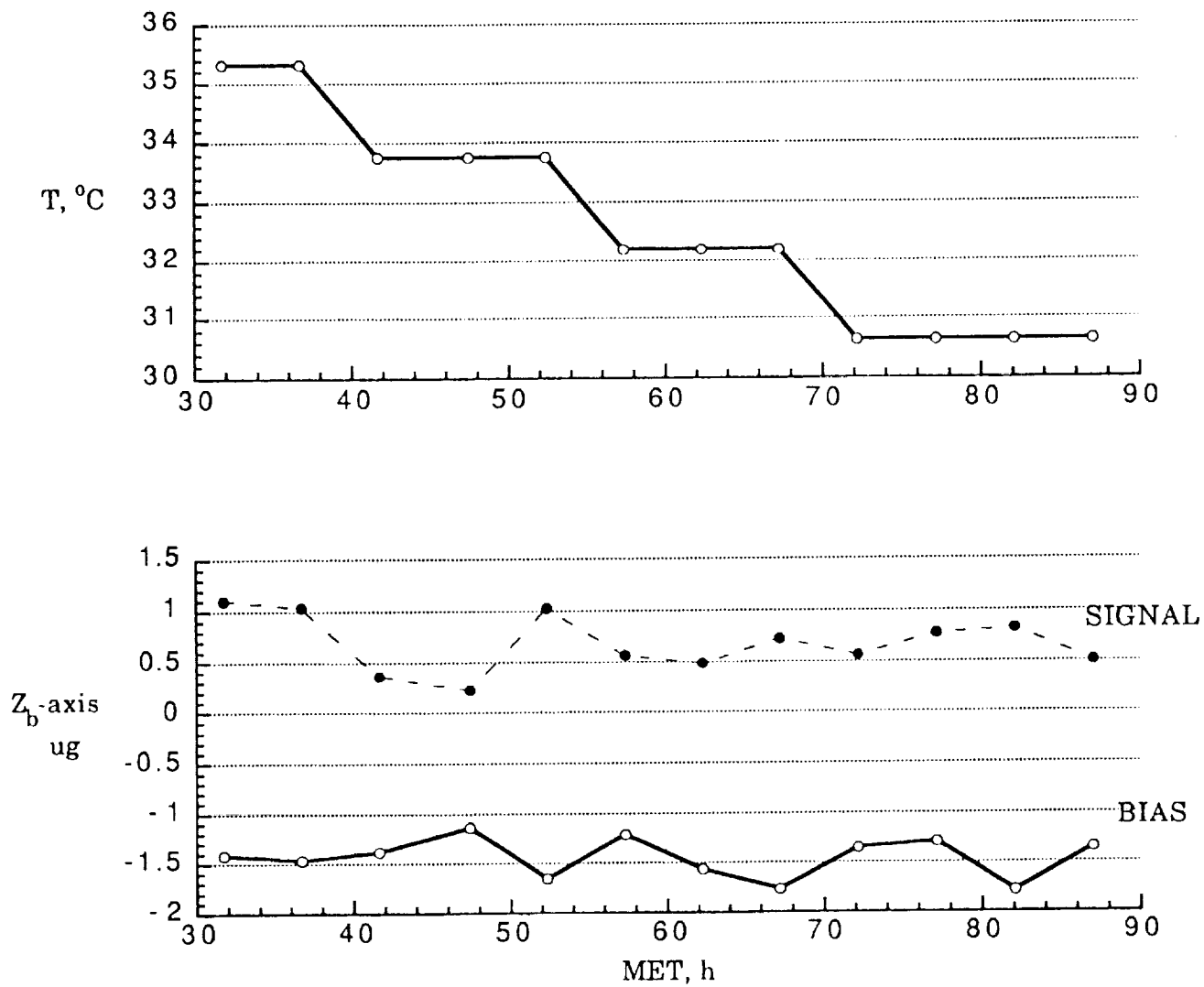


Figure 7 Z body axis sensor temperature, bias, and signal measurements.

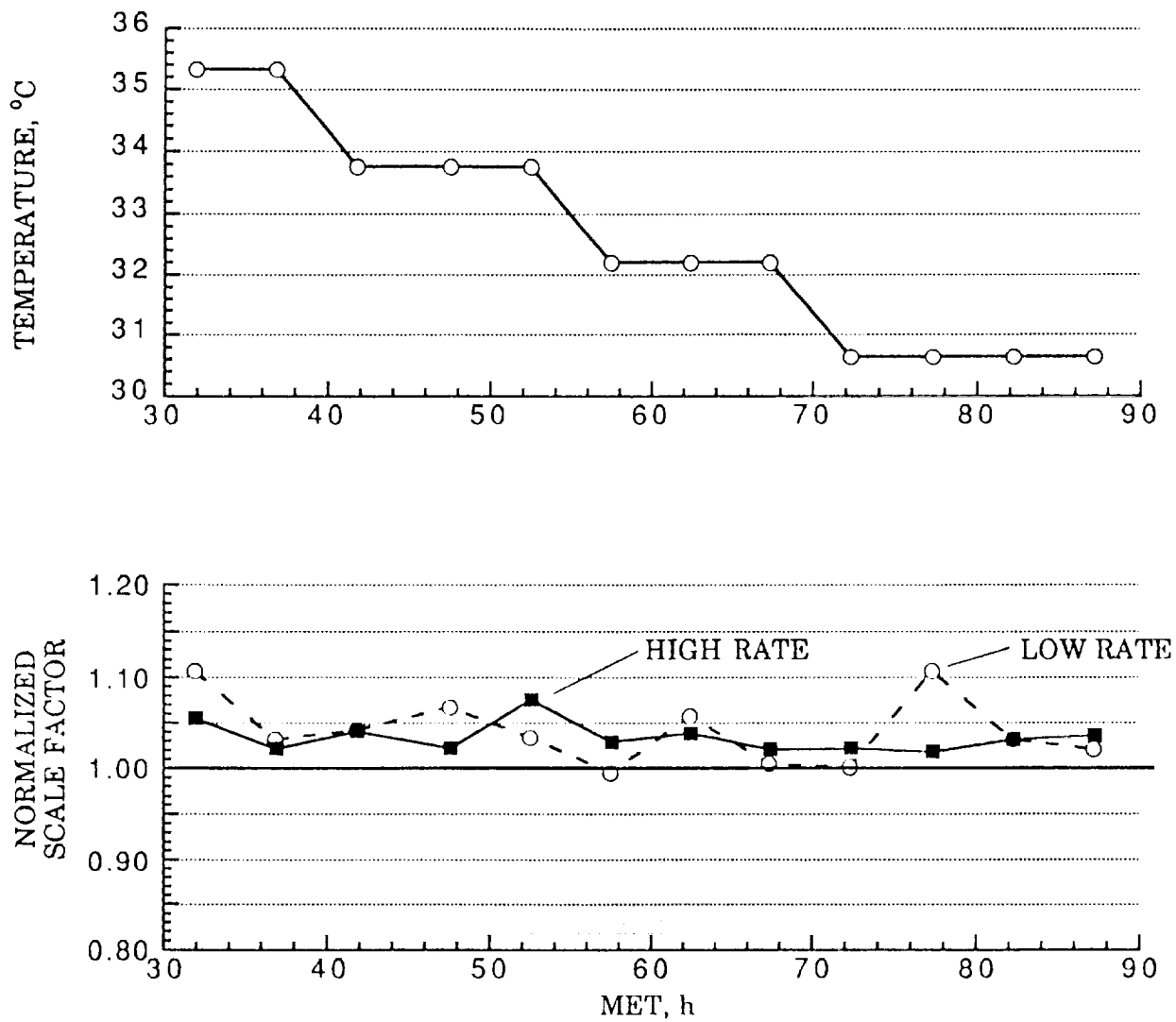


Figure 8 X-axis C-range scale factor measurements.

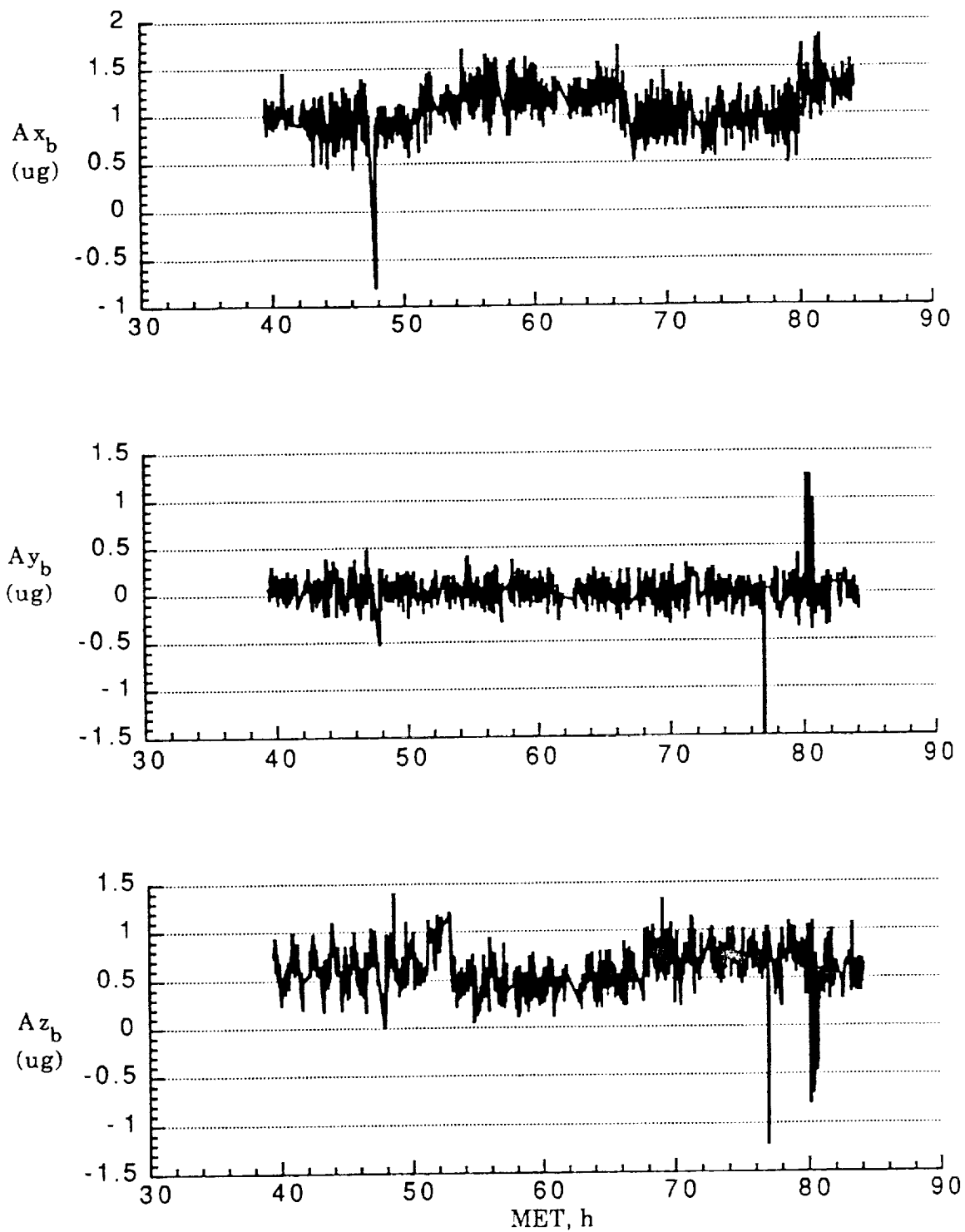


Figure 9 OARE body axes measurements at the OARE location.

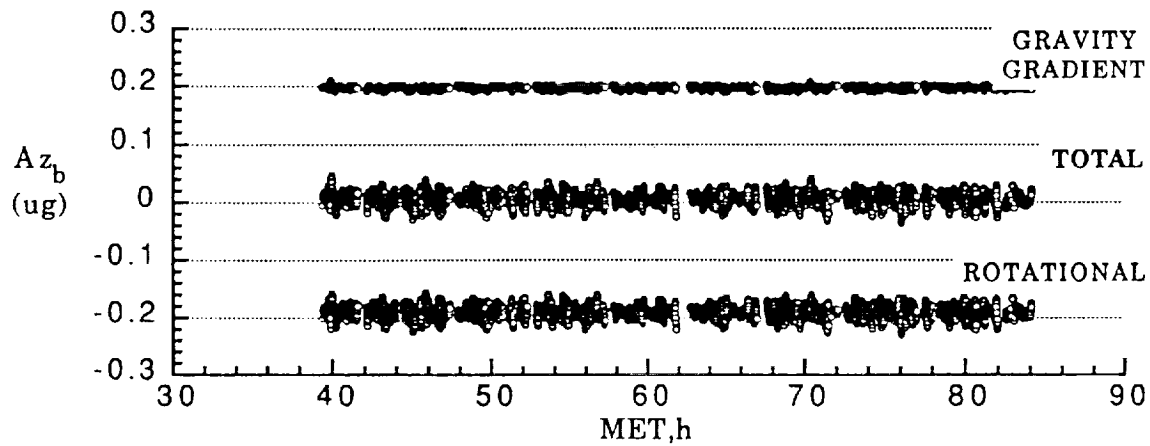
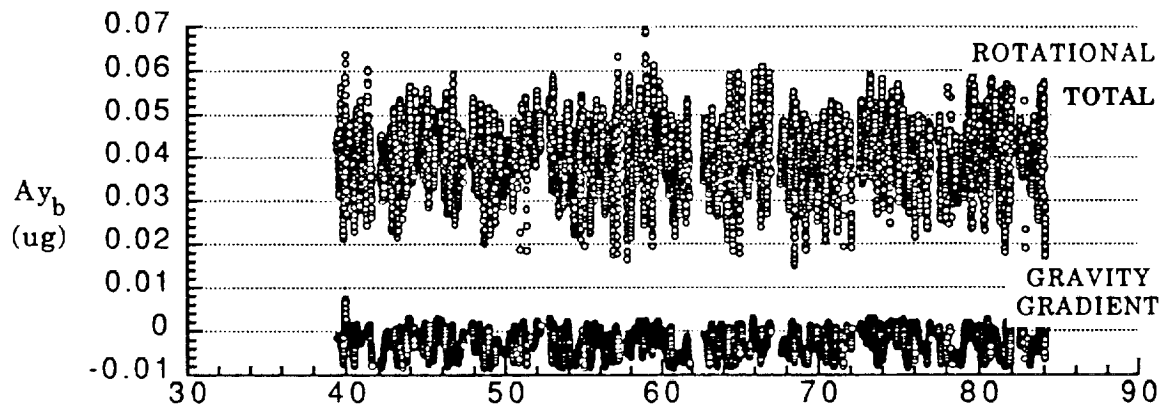
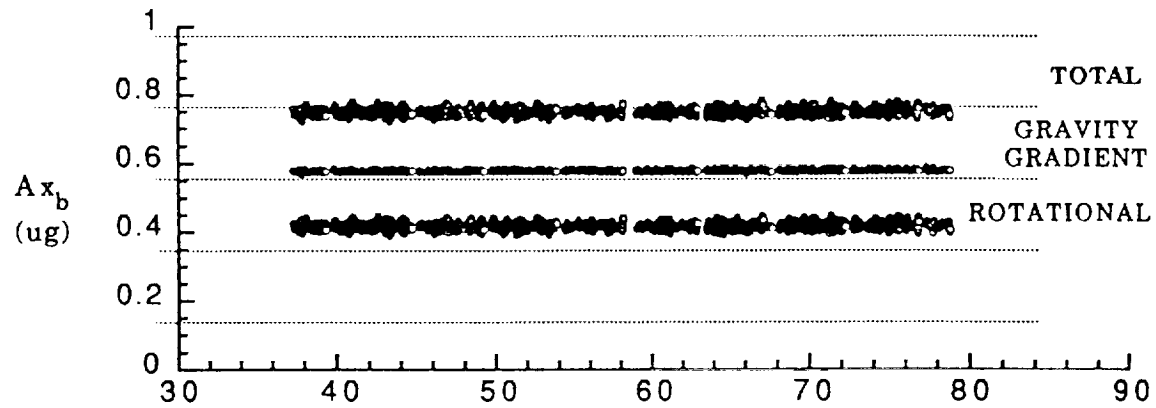


Figure 10 Gravity gradient and rotational accelerations from Orbiter measurements at the OARE location.

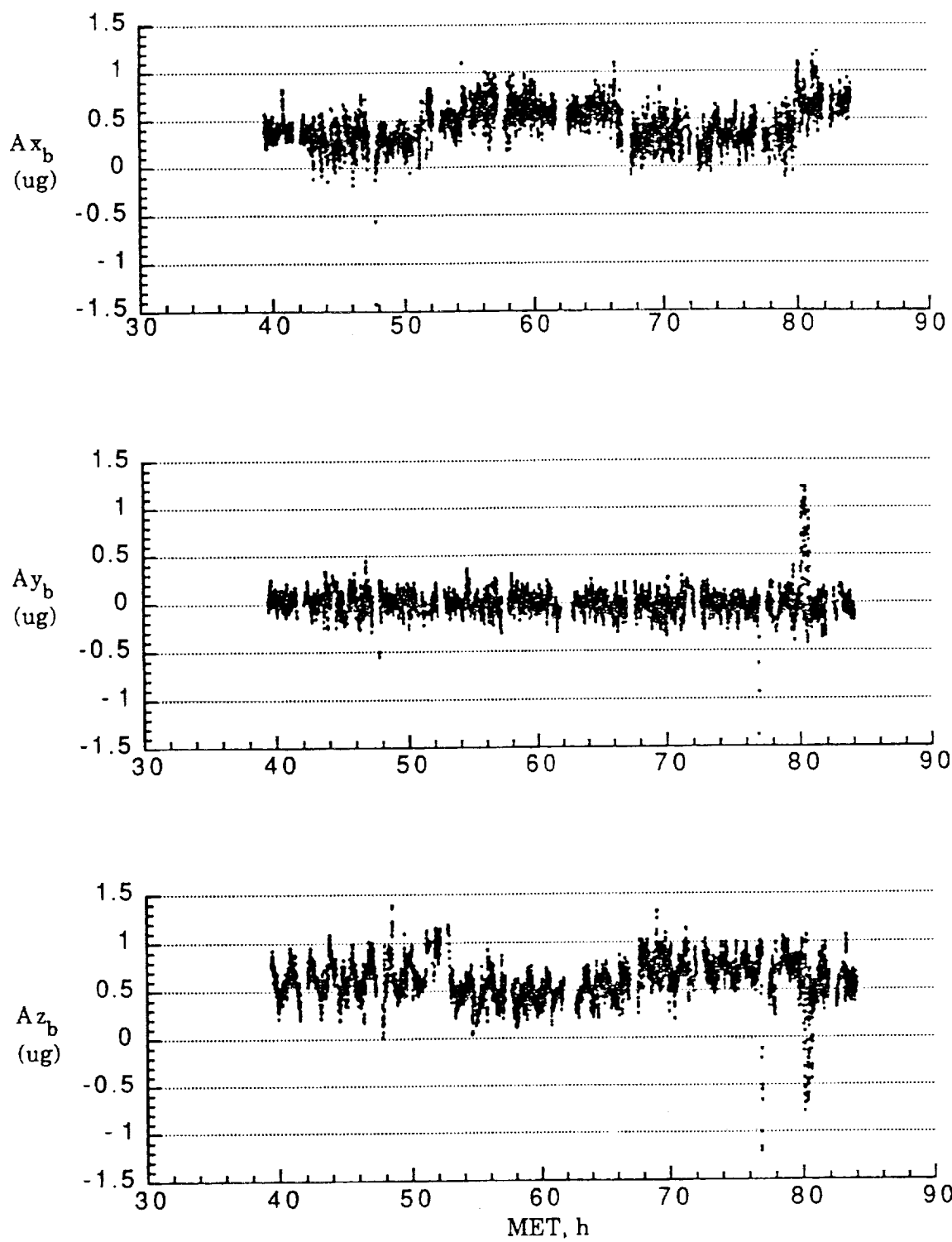


Figure 11 OARE measurements at the center of gravity.

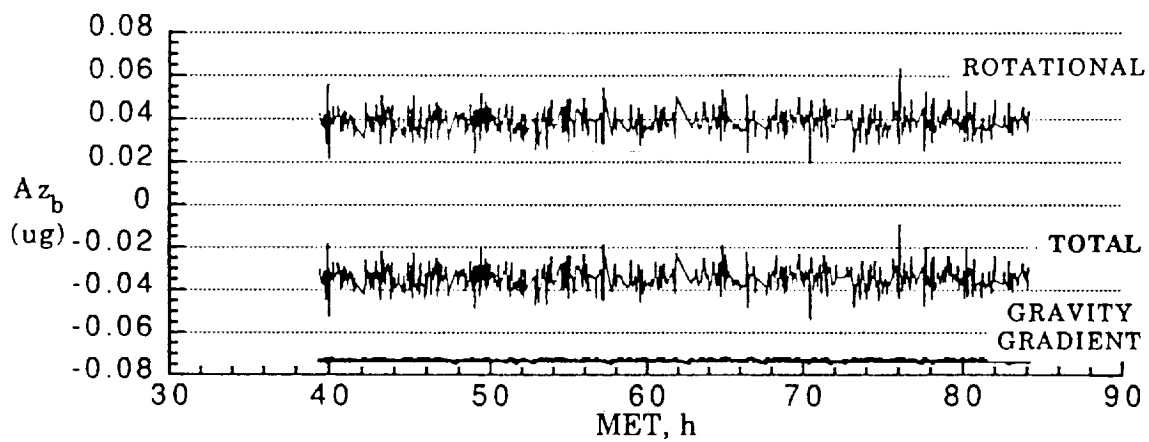
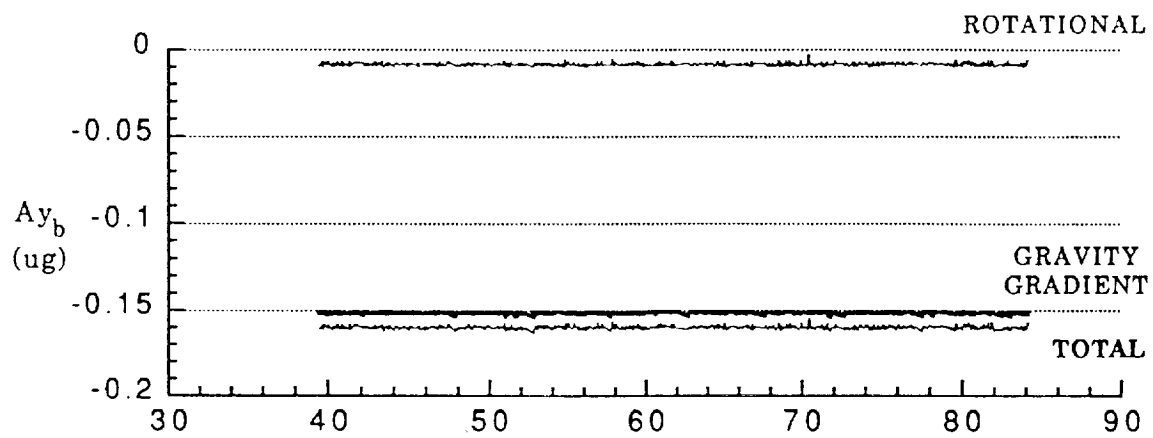
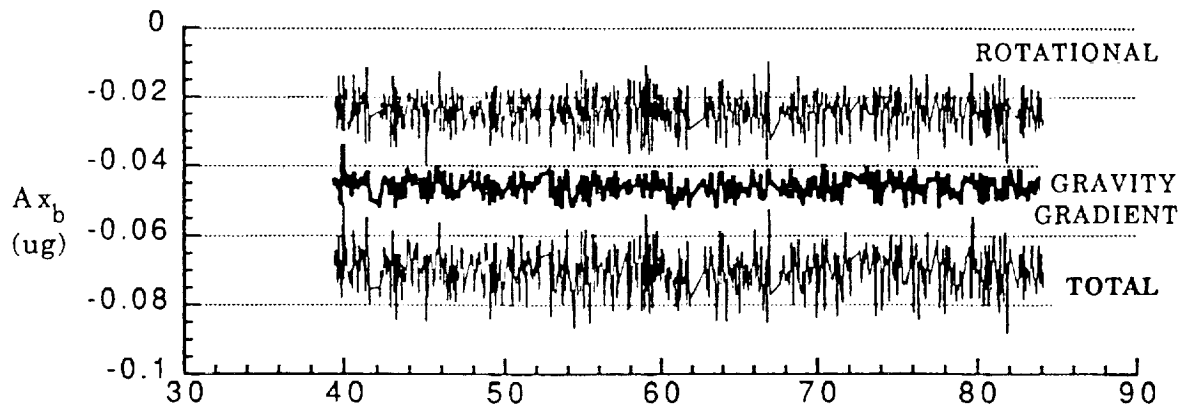


Figure 12 Gravity gradient and rotational accelerations from Orbiter measurements at the CGF location.

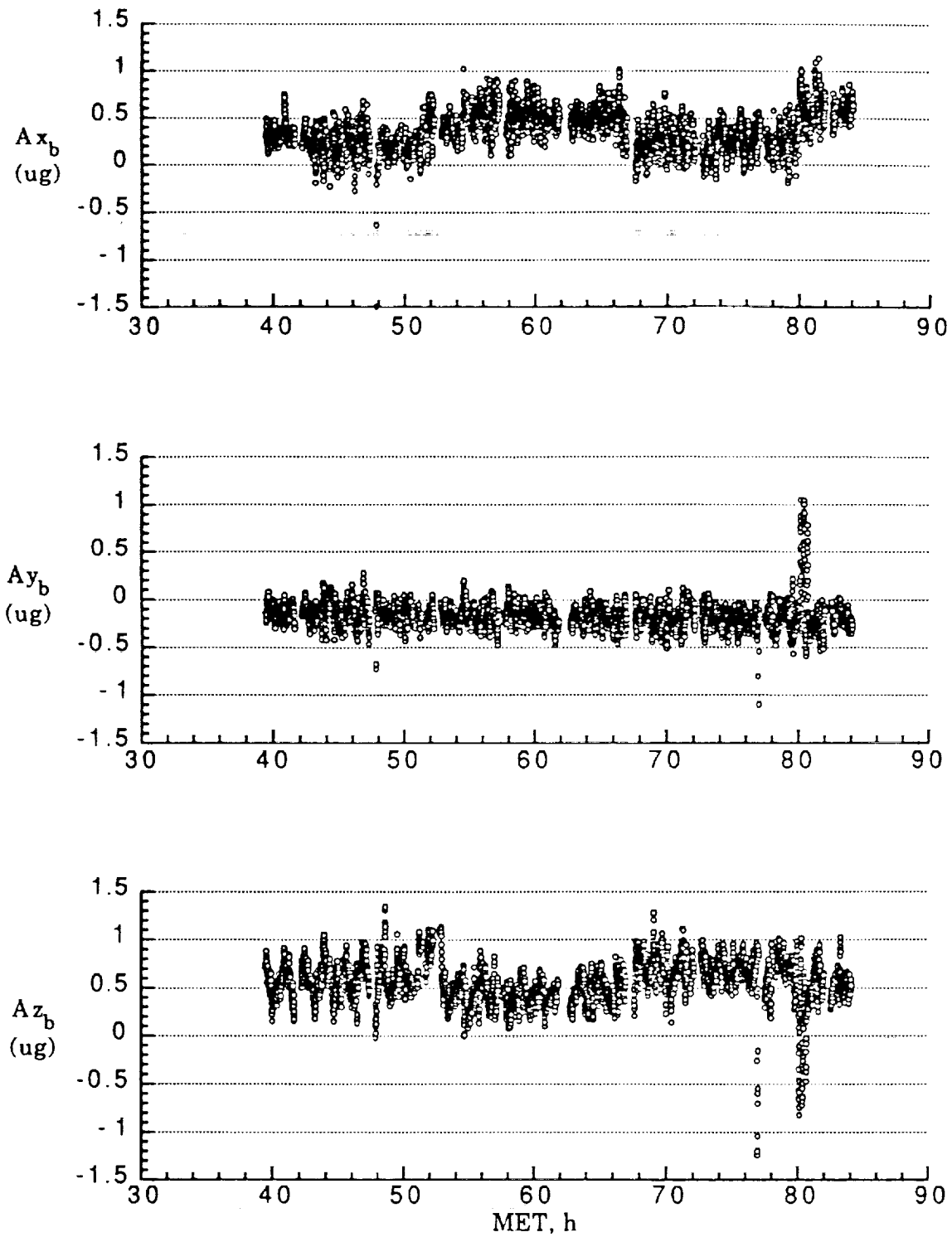


Figure 13 Body axes accelerations at the CGF location ($X_o = 1086.00$, $Y_o = 44.39$, $Z_o = 395.45$) using OARE data.

Discussion

Question: *Is the Flash Evaporation System (FES) the only contributing factor or are there several others that contributed to the measured residual g-levels ?*

Answer: Yes. There is more than just the FES. There are more things that are happening that need to come out and you could not see it on the charts that I showed you because the chart showed you 14 days of data. But if you look at details at various sections on the flight you see that there are more activities ongoing.

Question: *On the z axis data, especially the drag component, were they pretty well what you thought they should be ? Have you looked at that ?*

Answer: Well they are off because of the FES; we have yet to take it out. You saw on the chart I had up earlier, it was off by a factor of 2 or 3 because of the FES.

Question: *If that variation (z-axis data) is in phase with the day/night variation, it could be induced by different rates of out-gassing produced by the sun, i.e. temperatures. Have you examined that scenario ?*

Answer: Yes. That is a good observation. We modeled out gassing as best we can but the values you get are much too big. These values are tenths of a micro-g whereas out-gassing, we feel, will be less than that number, about an order of magnitude less.

Question: *What value of C_D did you pick for your model; 2.3 for all directions ?*

Answer: Yes we used a value of 2.3 but not for all directions. We used a complex model which has all angle of attack variations.

Question: *Do you know enough about the FES to know whether a quick fix will be the feasible thing to do or would you have a recommendation for that ?*

Answer: It doesn't bother me now that I know about it. Now I know where to look so I can look at those moments of the mission when the FES system was off and probably get enough data to satisfy myself and do the calculations I wanted to do. Certainly for people who are worried about the d.c. acceleration levels, that are on the order of $0.2 \mu g$ and that affects their experiments, they had better know when that system (FES) is operating because it may produce results that they are not happy with, for that experiment. For my experiment I can go and find the time when it was not operating but I am not sure that is true about everybody's experiment.

